# Hygro-thermo-mechanical modeling of thin-walled photovoltaic laminates with polymeric interfaces

Z. Liu [a,b,*], J. Reinoso [b], M. Paggi [a]

[a] *IMT School for Advanced Studies Lucca, Piazza San Francesco 19, 55100, Lucca, Italy*
[b] *Departamento de Mecánica de Medios Continuos y Teoría de Estructuras, School of Engineering, Universidad de Sevilla, Camino de los Descubrimientos s/n, 41092, Seville, Spain*

## ARTICLE INFO

## ABSTRACT

A three-dimensional hygro-thermo-mechanical computational framework for photovoltaic (PV) laminates as well as its numerical implementation are established in this work. Aiming at an efficient thermo-mechanical modeling of thin-walled structures with polymeric interfaces, the solid shell element, which incorporates the enhanced assumed strain (EAS) method and the assumed natural strain (ANS) method for the alleviation of locking pathologies, and the interface element with thermo-visco-elastic cohesive zone model using fractional calculus are formulated. Besides, the finite element (FE) implementation of moisture diffusion in the 3D setting along the polymeric interfaces is also derived with the consideration of spatial and temporal variation of diffusivity due to its temperature and material decohesion dependencies. Given the difference between the time scales of moisture diffusion and thermo-mechanical problems, a staggered scheme is proposed for the solution of the coupled hygro-thermo-mechanical governing equations. Specifically, the relative displacement and temperature fields are firstly solved from the thermo-mechanical analysis, and then projected to the FE model of moisture diffusion to determine the diffusion coefficient for its subsequent analysis. The proposed method is applied to the simulation of three international standard tests of PV modules, namely the damp heat test, the humidity freeze test, and the thermal cycling test, and numerical predictions are compared with analytical solution for the damp heat case with a constant temperature boundary condition, as well as experimental electroluminescence (EL) images obtained from the thermal cycling test with the cyclic temperature boundary condition. A very satisfactory consistency demonstrates the effectiveness and reliability of this modeling framework.

## 1. Introduction

Typical photovoltaic modules are laminates consisting of different layers, including tempered glass, encapsulant layers (usually ethylene vinyl acetate, EVA), a layer of interconnected silicon solar cells, and backsheet, see Fig. 1. The layer of silicon solar cells is used to produce electric energy, while the other layers like glass and backsheet play the role of protecting the modules from the outdoor harsh environments (Deng et al., 2021). The durability analysis of PV modules has received a great deal of attention in the past decades (Liu et al., 2022a; Gagliardi and Paggi, 2019; Antartis and Chasiotis, 2014; Lenarda and Paggi, 2016), and the modeling of polymeric materials is quite challenging as it requires a multiphysics framework to accurately predict their overall performance and degradation (Paggi et al., 2013; Bahrololoumi et al., 2020, 2021; Silberstein and Boyce, 2010, 2011).
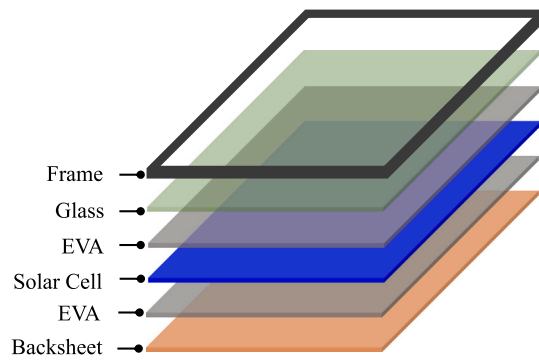
---

**Fig. 1.** The general structure of a typical PV module (Liu et al., 2022a).
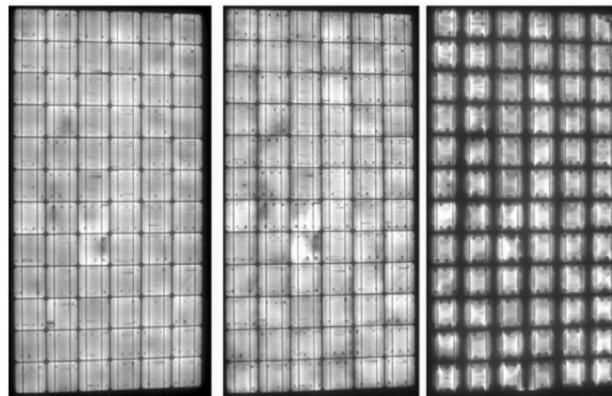


**Fig. 2.** EL images of PV modules with moisture induced dimmer areas during the damp heat test (Herrmann and Bogdanski, 2011).

The EVA layer of PV modules is usually made of polymeric materials, and permeable to moisture, which diffuses from the edges, backsheet and interspaces between different solar cells. This moisture diffusion can induce chemical oxidation of grid lines deposited on the surface of solar cells and subsequently lead to degradation and power loss, which has been reported in the damp heat test of PV modules exposed to the very aggressive environment with 85 °C temperature and 85% relative humidity (Iseghem et al., 2012; Köntges et al., 2017, 2014). As shown in Fig. 2, the dark bands can be observed at the edges of solar cells in the captured EL image after different elapsed time, which were not detected in the beginning but became evident during ageing. It is important to remark that in photovoltaics, the larger the dark – electrically inactive – area, the higher the electrical power loss of the module, see Paggi et al. (2016). Particularly, in the damp heat accelerated ageing test, the dark bands relate to the moisture ingress into the module from the edges of the solar cells over time. Since moisture can induce chemical reactions inside the modules and delamination failure between different laminae, it is crucial to establish a reliable and accurate modeling strategy of moisture diffusion along the EVA layer. The complexity regards the strong dependency of moisture diffusion coefficient of EVA on the temperature, which indicates the coupling between the moisture and thermal fields, as shown in Kempe (2006). On the other hand, moisture diffusion also degrades the cohesive energy of EVA layer, giving rise to the delamination failure between the different laminae (Liu et al., 2019), such as the decohesion between solar cell and backsheet or tempered glass (Novoa et al., 2014, 2016), which corresponds to the coupling between the mechanical and moisture fields (Dunlop, 2003).

Regarding the thermo-mechanical behavior, the EVA polymer shows a strong thermo-visco-elastic constitutive response, and its Young's modulus varies within a range by three orders of magnitude depending on temperature, as experimentally reported in Eitner et al. (2011), Paggi et al. (2011). In order to approximate the power-law trend from experimental observation, the generalized Maxwell rheological models can be used to determine the relaxation modulus with exponential type equations. However, a great number of elements as well as model parameters have to be taken into account, which requires laborious calibration work. To simplify the procedure of parameter identification, the fraction calculus method has been proved to be very effective for the modeling of visco-elastic constitutive behavior (Mainardi, 2010; Di Paola et al., 2013, 2011). Thus this formulation has been adopted to describe the rheologically complex behavior of polymeric EVA, whose microstructure changes with temperature, and, according to Paggi and Sapora (2015), only two temperature dependent parameters are required for its complete description.

To model these coupled nonlinear hygro-thermo-mechanical problems in PV modules, a comprehensive computational framework in the three-dimensional space, where the coupled thermo-mechanical problem and the moisture diffusion are solved in a staggered manner, is required so that the dependency of diffusion properties of EVA on the thermo-mechanical fields can be accounted for
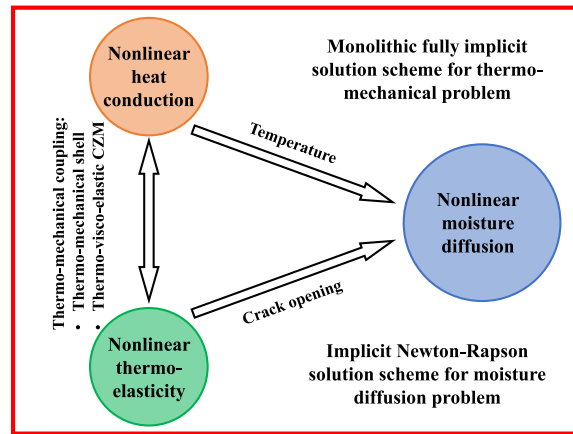
**Fig. 3.** The proposed solution scheme for the 3D hygro-thermo-mechanical modeling framework.

properly. Analytical solution for the moisture diffusion along EVA layer proposed in Kempe (2006) assumes constant diffusivity without any update based on the actual temperature, and the spatial variation due to temperature dependency is ignored. Although it might be feasible in the steady state temperature case, such as in the damp heat test, its validity for cyclic temperature boundary conditions in the humidity freeze and in the thermal cycling tests is hard to guarantee. Besides, since moisture can also diffuse from the channel cracks and interspaces between the solar cells, it is almost impossible to obtain analytical solution in these complex cases. To overcome the limitations of analytical solution methods, the finite element modeling methodology in the three-dimensional setting is proposed to simulate the coupled problems in this work. The thermo-mechanical phenomena in the PV laminate, which is much faster than moisture diffusion, is firstly solved through a monolithic fully implicit solution scheme, see Fig. 3. The calculated temperature and displacement fields inside the EVA layer are then projected to the nodes of another finite element model specific for moisture diffusion, so that the diffusion properties at the corresponding time and space can be determined accordingly. With updated diffusion coefficient from thermo-mechanical solution at each time increment, the moisture diffusion can be solved by the Newton–Raphson scheme in a standard way.

For the sake of computational efficiency, the EVA layers are modeled using zero-thickness interface finite elements with a thermo-visco-elastic cohesive zone model based on fractional calculus, and a thermo-mechanical solid shell formulation incorporating the EAS and ANS methods to remedy potential locking pathologies, which is kinematically compatible with the 3D interface element, is established here for the modeling of the different thin-walled laminae in PV modules such as glass layer, backsheet and silicon solar cell layer. Modeling thermo-mechanical responses in thin-walled structures necessitates the consistent derivation of formulations accounting for the stress and heat transfer across the internal interfaces. To use the 3D constitutive laws without further modifications, recent advances in shell element formulation aim at incorporating the three-dimensional effects into the corresponding implementation. To achieve this, it is pointed out in Rah et al. (2013), Vu-Quoc and Tan (2003) that a linear normal strain distribution through the thickness direction has to be embodied in the shell element formulation. In this regard, two paths have been followed: (i) shell formulations that include the linear distribution using either quadratic displacement distribution or enhanced strain methods through the reference surface of body in the thickness direction (Başar and Ding, 1997; Betsch et al., 1996; Brank, 2005; Büchter et al., 1994; Parisch, 1995; Simo et al., 1990; Liu and Xia, 2021), and (ii) shell formulations relying on the solid shell concept through the parametrization of the top and bottom surfaces of the body (Miehe, 1998; Reinoso and Blázquez, 2016; Harnau and Schweizerhof, 2002; Klinkel and Wagner, 1997; Schwarze and Reese, 2009; Liu and Xia, 2019; Liu et al., 2022b). The latter has been extensively developed in the past decades since the complex update procedure regarding the rotation tensor can be completely avoided. However, the extension of solid shell formulation to thermo-mechanical applications has received very limited attention, see Braun et al. (1994), Bathe and Dvorkin (1985), Bischoff and Ramm (1997), Hauptmann et al. (2000). Besides, to alleviate the locking pathologies in shell formulations complying with the low-order kinematic interpolation, different numerical strategies have been proposed such as the EAS method (Korelc and Wriggers, 1996; Simo et al., 1993; Simo and Rifai, 1990; Valente et al., 2003), the ANS method (Betsch and Stein, 1995; Dvorkin and Bathe, 1984), and combination of them (Cardoso et al., 2008; Gruttmann and Wagner, 2006; Kasper and Taylor, 2000).

This work is structured as follows. In Section 2, the primary aspects of coupled thermo-mechanical analysis along with the definition of kinematics and constitutive formulation, the thermo-visco-elastic cohesive zone model through the fractional calculus method, as well as temperature and gap dependent moisture diffusion are presented in detail. The weak forms of the governing equations for the hygro-thermo-mechanical problems and the corresponding finite element discretization are given in Section 3. In particular, the Hu–Washizu variational principle with thermo-mechanical solid shell formulation accounting for the EAS and ANS methods to alleviate locking effects is outlined in Section 3.1, while Section 3.2 and Section 3.3 cover the 3D thermo-mechanical interface and moisture diffusion finite element implementation, respectively. Details of the numerical algorithm for the implementation of the hygro-thermo-mechanical framework with staggered solution scheme are provided in Section 4. Then
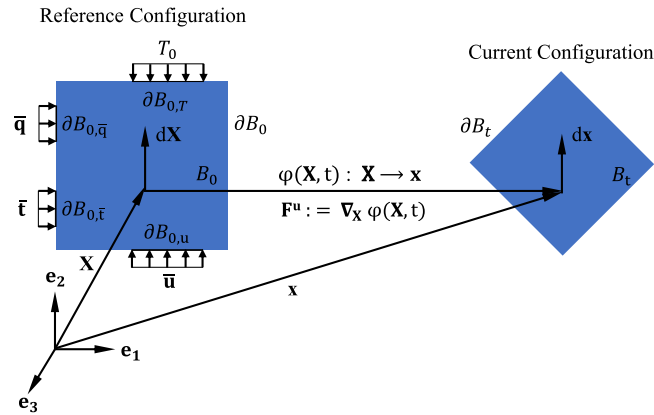
**Fig. 4.** The finite thermo-mechanical deformation of a three-dimensional body from the reference configuration to the current configuration.

this modeling methodology is applied to simulate the three international standard tests of PV laminates, and validated with the analytical solution as well as experimental data, which is presented in Section 5. Finally, some concluding remarks of the proposed modeling framework are drawn in Section 6.

## 2. Hygro-thermo-visco-elastic modeling framework for the PV laminate

In this section, the modeling framework for the thermo-mechanical coupling in thin-walled PV laminae separated by thermo-visco-elastic interfaces and moisture diffusion along the polymeric layers is presented. Moisture diffusion takes place in the polymeric encapsulant layers of laminate, which usually percolates from the free edges and towards the center of solar cell panels. The encapsulant layers are made of visco-elastic polymer materials and permeable to moisture, which is one of the dominant factors leading to the electrical degradation of PV modules during the service life. Besides, moisture diffusion can also degrade the adhesion strength of encapsulant layers, causing delamination failure between silicon solar cells and backsheet or the glass superstrate. In order to effectively model the cohesive mechanical behavior of encapsulant layers, a 3D cut-off traction–separation law is formulated.

### 2.1. Coupled thermo-mechanical kinematics and formulation

For thermo-mechanical boundary value problems in solids, displacement and absolute temperature fields are usually chosen as the independent fields in the coupled governing equations. In the 3D setting, let $\mathcal{B}_0 \subset \mathbb{R}^3$ denotes the reference configuration, while $\mathcal{B}_t \subset \mathbb{R}^3$ denotes the current configuration. The position vectors of material points in the reference and current configurations are represented by $\mathbf{X}$ and $\mathbf{x}$, respectively. The displacement field is denoted as $\mathbf{u}(\mathbf{X}, t) : \mathcal{B}_0 \times [0, t] \to \mathbb{R}^3$, which is a vector valued function during the time interval $[0, t]$. The absolute temperature field $T(\mathbf{X}, t) : \mathcal{B}_0 \times [0, t] \to \mathbb{R}_+$ is a smooth scalar-value function. As shown in Fig. 4, the body motion denoted by $\boldsymbol{\varphi}(\mathbf{X}, t) : \mathcal{B}_0 \times [0, t] \to \mathbb{R}^3$ maps the material point $\mathbf{X}$ in the reference configuration onto its corresponding point $\mathbf{x}$ in the current configuration.

The mechanical boundary conditions are imposed on the boundary of deformable body in the reference configuration $\partial \mathcal{B}_0$, which is divided by disjoint sets $\partial \mathcal{B}_{0,u} \subset \partial \mathcal{B}_0$ and $\partial \mathcal{B}_{0,\bar{t}} \subset \partial \mathcal{B}_0$ with $\partial \mathcal{B}_{0,u} \cap \partial \mathcal{B}_{0,\bar{t}} = \emptyset$. The Dirichlet boundary condition $\mathbf{u} = \bar{\mathbf{u}}$ is applied on $\partial \mathcal{B}_{0,u}$, while Neumann boundary condition characterized by prescribed tractions $\boldsymbol{\sigma} \cdot \mathbf{n} = \bar{\mathbf{t}}(\mathbf{X}, t)$ is applied on $\partial \mathcal{B}_{0,\bar{t}}$. Similarly, the temperature boundary condition $T = T_0$ is prescribed over $\partial \mathcal{B}_{0,T} \subset \partial \mathcal{B}_0$, while the heat flux boundary condition $q = \bar{q}$ is prescribed over $\partial \mathcal{B}_{0,\bar{q}} \subset \partial \mathcal{B}_0$, such that $\partial \mathcal{B}_{0,T} \cap \partial \mathcal{B}_{0,\bar{q}} = \emptyset$. Besides, the deformable body can also be divided into parts $\mathcal{B}_0^i (i > 0)$ such that $\mathcal{B}_0 = \cup_i \mathcal{B}_0^i$, which could be assigned with different mechanical and thermal constitutive behaviors.

The deformation gradient, which is defined as the gradient of deformation map with regard to the reference configuration, can be expressed as

$$\mathbf{F}^u := \partial_{\mathbf{X}} \boldsymbol{\varphi}(\mathbf{X}, t) = \nabla_{\mathbf{X}} \boldsymbol{\varphi}(\mathbf{X}, t), \tag{1}$$

where $\nabla_{\mathbf{X}}[\bullet]$ denotes the Lagrangian gradient operator. This operator represents the map of line element $d\mathbf{X}$ in the reference configuration onto the corresponding line element $d\mathbf{x} = \mathbf{F}^u d\mathbf{X}$ in the current configuration. The Jacobian of the deformation is defined as the determinant of deformation gradient $J^u := \det[\mathbf{F}^u] > 0$, where $\det[\bullet]$ represents the determinant operator.

The covariant tangent vectors $\mathbf{G}_i(\xi)$ and $\mathbf{g}_i(\xi)$ are defined as the partial derivatives of position vectors with respect to the convective coordinates $\xi^i$ in the reference and current configurations, respectively

$$\mathbf{G}_i(\xi) := \frac{\partial \mathbf{X}(\xi)}{\partial \xi^i}, \quad \mathbf{g}_i(\xi) := \frac{\partial \mathbf{x}(\xi)}{\partial \xi^i}, \quad i = 1, 2, 3. \tag{2}$$

The contravariant vectors are defined by $\mathbf{G}_i \cdot \mathbf{G}^j = \delta_i^j$ and $\mathbf{g}_i \cdot \mathbf{g}^j = \delta_i^j$, and the metric tensors are defined as $\mathbf{G} = G_{ij}\mathbf{G}^i \otimes \mathbf{G}^j = G^{ij}\mathbf{G}_i \otimes \mathbf{G}_j$, $\mathbf{g} = g_{ij}\mathbf{g}^i \otimes \mathbf{g}^j = g^{ij}\mathbf{g}_i \otimes \mathbf{g}_j$. The left and right Cauchy–Green deformation tensors, which are derived from displacement field vectors, are given by

$$\mathbf{C}^u := [\mathbf{F}^u]^{\mathrm{T}}\mathbf{g}[\mathbf{F}^u], \quad \mathbf{b}^u := [\mathbf{F}^u]\mathbf{G}^{-1}[\mathbf{F}^u]^{\mathrm{T}}. \tag{3}$$

The Green–Lagrange strain tensor $\mathbf{E}^u$ is defined as

$$\mathbf{E}^u := \frac{1}{2}\left[\mathbf{C}^u - \mathbf{G}\right]. \tag{4}$$

In order to alleviate the locking effects according to Bischoff and Ramm (1997), an incompatible strain tensor $\tilde{\mathbf{E}}$ is incorporated into the displacement derived quantities, and the total Green–Lagrange strain by additive decomposition takes the form of

$$\mathbf{E} := \mathbf{E}^u + \tilde{\mathbf{E}}. \tag{5}$$

This decomposition constitutes the fundamentals of assumed strain method, and thus the enhanced right Cauchy–Green tensor $\mathbf{C}$ is given by

$$\mathbf{C} := \mathbf{C}^u + \tilde{\mathbf{C}} = 2(\mathbf{E}^u + \tilde{\mathbf{E}}) + \mathbf{G}. \tag{6}$$

Then the enhanced deformation gradient $\mathbf{F}$ can be derived by the polar decomposition theorem. The displacement derived deformation gradient can be decomposed as $\mathbf{F}^u := \mathbf{R}\mathbf{U}^u$, where $\mathbf{R}$ and $\mathbf{U}^u$ represents the rotation and right-stretch tensors, respectively. Based on Eq. (6), the modified right-stretch tensor $\mathbf{U}$ that accounts for the incompatible strain is calculated as

$$\mathbf{U} := \sqrt{\mathbf{C}}. \tag{7}$$

Since the calculation of rotation tensor is straightforward, the modified deformation gradient $\mathbf{F}$ can be computed as

$$\mathbf{F} := \mathbf{R}\mathbf{U}. \tag{8}$$

The modified corresponding Jacobian is given by $J = \det[\mathbf{F}]$.

Consider $\mathcal{P}_0 \subset \mathcal{B}_0$ from the continuum body $\mathcal{B}_0$ in the reference configuration with the delimiting boundary $\partial\mathcal{P}_0$, and its spatial counterpart $\mathcal{P}_t \subset \mathcal{B}_t$, with the boundary $\partial\mathcal{P}_t$ in the current configuration. It is postulated in Cauchy stress theorem that there is a linear dependency between the normal vector $\mathbf{n}$ of $\partial\mathcal{P}_t$ and traction $\mathbf{t}$ through Cauchy stress tensor $\boldsymbol{\sigma}$, which is given by

$$\mathbf{t} = \boldsymbol{\sigma} \cdot \mathbf{n}. \tag{9}$$

In line with this theorem, the first Piola–Kirchhoff stress tensor $\mathbf{P}$, which is also known as nominal stress tensor, is defined as

$$\mathbf{P} = J\boldsymbol{\sigma} \cdot \mathbf{F}^{-1}. \tag{10}$$

The first Piola–Kirchhoff traction vector $\hat{\mathbf{T}}$ is defined as $\hat{\mathbf{T}} = \mathbf{P} \cdot \mathbf{N}$, which satisfies the force equality $\hat{\mathbf{T}}\mathrm{d}S = \mathbf{t}\mathrm{d}s$, and $\mathbf{N}$ denotes the normal direction in the reference configuration. Accordingly, the second Piola–Kirchhoff stress tensor $\mathbf{S}$, which is a symmetrical stress tensor, is given by

$$\mathbf{S} = \mathbf{F}^{-1} \cdot \mathbf{P} = J\mathbf{F}^{-1} \cdot \boldsymbol{\sigma} \cdot \mathbf{F}^{-1}. \tag{11}$$

Analogously, Stokes heat flux theorem in the current configuration reads

$$q_n = \mathbf{q} \cdot \mathbf{n}, \tag{12}$$

where $q_n$ and $\mathbf{q}$ represent the scalar and vector heat flux, respectively, and $\mathbf{n}$ denotes the normal direction in the current configuration. The material heat flux $\mathbf{Q}$ can be determined from the equality condition $\mathbf{q} \cdot \mathbf{n}\mathrm{d}s = \mathbf{Q} \cdot \mathbf{N}\mathrm{d}S$, and thus its definition can be expressed as

$$\mathbf{Q} = J\mathbf{F}^{-1} \cdot \mathbf{q}. \tag{13}$$

Recalling the theoretical developments outlined in Weber and Anand (1990), Bargmann and Steinmann (2006), the Helmholtz free energy function for the thermo-elastic Kirchhoff–Saint-Venant constitutive material law is given by

$$\Psi(\mathbf{E}, T) = \frac{1}{2}\lambda\left(\mathrm{tr}[\mathbf{E}]\right)^2 + \mu\mathrm{tr}[\mathbf{E}^2] - 3\kappa\alpha\mathrm{tr}[\mathbf{E}]\left(T - T_0\right) + \rho_0 c_p\left[\left(T - T_0\right) - T\log\frac{T}{T_0}\right], \tag{14}$$

where $\kappa$ is the bulk modulus, $\lambda$ and $\mu$ are the Lame constants, $\rho_0$ is the mass density, $\alpha$ represents the thermal expansion coefficient and $T_0$ stands for the reference temperature.

The second Piola–Kirchhoff stress tensor can be obtained from the constitutive relationship, which reads

$$\mathbf{S} := \partial_{\mathbf{E}}\Psi = \lambda\left(\mathrm{tr}[\mathbf{E}]\right)\mathbf{1} + 2\mu\mathbf{E} - 3\kappa\alpha\left(T - T_0\right)\mathbf{1}, \tag{15}$$

where $\mathbf{1}$ is the second-order identity tensor. The constitutive operators in the curvilinear setting take the form

$$\mathbb{C} = \partial^2_{\mathbf{E}\mathbf{E}}\Psi = \left[\lambda G^{ij}G^{kl} + \mu\left(G^{ik}G^{jl} + G^{il}G^{jk}\right)\right]\mathbf{G}_i \otimes \mathbf{G}_j \otimes \mathbf{G}_k \otimes \mathbf{G}_l, \tag{16a}$$
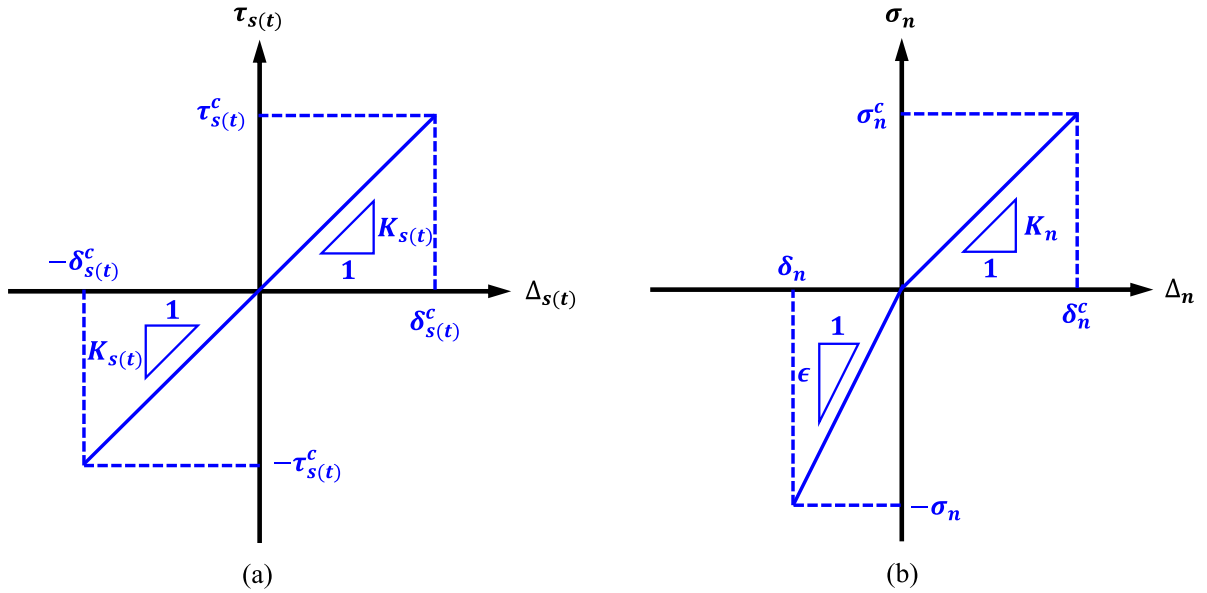
**Fig. 5.** The traction versus separation curves of the polymeric interface: (a) sliding and shearing modes, and (b) the opening mode.

$$\mathbf{Z} = \partial^2_{T\mathbf{E}}\Psi = -3\kappa\alpha G^{ij}\mathbf{G}_i \otimes \mathbf{G}_j. \tag{16b}$$

where $\mathbb{C}$ is the fourth-order material stiffness tensor, and $\mathbf{Z}$ is the second-order tensor associated with the coupling term of the Helmholtz function.

Assuming isotropic conductivity $\mathbf{k} = kg^{ij}\mathbf{g}_i \otimes \mathbf{g}_i$ (Kuhl et al., 2004), the material heat flux vector in the curvilinear setting can be expressed as

$$\mathbf{Q} = -J\mathbf{F}^{-1}\mathbf{k}\mathbf{F}^{-\mathrm{T}}\nabla_{\mathbf{X}}T = -Jk\left(\mathbf{G}_i \otimes \mathbf{g}^i\right)\left(g^{kl}\mathbf{g}_k \otimes \mathbf{g}_l\right)\left(\mathbf{g}^j \otimes \mathbf{G}_j\right)\nabla_{\mathbf{X}}T = -Jk\mathbf{C}^{-1}\nabla_{\mathbf{X}}T. \tag{17}$$

where $\mathbf{C}^{-1}$ stands for the inverse of right Cauchy–Green tensor. The formulation can be further simplified as $\mathbf{Q} = -k_0\mathbf{G}\nabla_{\mathbf{X}}T$ under isotropic assumption, where $k_0$ represents the thermal conductivity in the reference configuration.

### 2.2. Thermo-visco-elastic cohesive interface model of polymeric layers

Assuming that the polymeric layers can be treated as zero-thickness imperfect interfaces, the displacement and temperature fields inside the encapsulant layers are allowed to be discontinuous through the thickness direction. The cohesive zone model assumes the existence of free energy density per unit undeformed area, and thermo-mechanical coupling can be achieved by making conductivity properties dependent on the cohesive damage and interface tractions dependent on the temperature field. Let define the displacement gaps along the interfaces in three-dimensional setting as: $\mathbf{\Delta} = (\Delta_n, \Delta_t, \Delta_s)$, where $\Delta_n, \Delta_s, \Delta_t$ stand for normal, tangential and shear displacement gaps, respectively, and temperature gap $\Delta_T$ along the interface, which play the role of internal variables for the description of the debonding process along polymeric interfaces.

Hence, the coupled thermo-mechanical model for deformable laminae body is enriched due to the presence of cohesive traction field and heat flux through the thickness direction of polymeric layer. Under the assumption of continuity along the interface, the out-of-plane tearing and in-plane sliding traction vectors are defined as

$$\tau_I = \begin{cases} K_I(t,\langle T\rangle)\Delta_I, & \text{if } \Delta_I \in J_I \\ 0, & \text{if } \Delta_I \notin J_I \end{cases} \tag{18}$$

where $J_I = \left(-\delta^c_I, +\delta^c_I\right)$, $\langle T\rangle$ is the average temperature along the interface and $I = t, s$, while the opening traction component $\sigma$ is defined as

$$\sigma = \begin{cases} \epsilon\Delta_n, & \text{if } \Delta_n < 0 \\ K_n(t,\langle T\rangle)\Delta_n, & \text{if } \Delta_n \in J_n \\ 0, & \text{if } \Delta_n \notin J_n \text{ and } \Delta_n \geq 0 \end{cases} \tag{19}$$

where $J_n = \left(0, \delta^c_n\right)$, and $\epsilon$ is the penalty parameter in compression (Corrado and Paggi, 2015). This corresponds to a tension cut-off traction separation cohesive law, in which the interface cannot transfer tractions when the critical opening gap $\delta^c_n$ is reached. The similar brittle behavior is assumed for the tearing and sliding modes, see Fig. 5.

To obtain the structural response of encapsulant layers, the stiffness $K_n$ is related to the actual stiffness of polymeric materials in the normal direction, which is calculated as the ration between the Young's modulus $E_{poly}$ and its thickness $h_{poly}$, i.e., $K_n = E_{poly}/h_{poly}$. Analogously, the tearing and sliding stiffness can be expressed as: $K_s = K_t = E_{poly}/[2h_{poly}(1 + v_{poly})]$. Since polymeric materials have thermo-visco-elastic constitutive behaviors, the Young's modulus $E_{poly}$ depends both on the average temperature $\langle T \rangle$ and time history $t$. To synthetically characterize these dependencies, a fractional calculus approach proposed in Di Paola et al. (2013) is adopted here instead of the use of Prony series representation, which has been proved to be very effective for parameters identification (Paggi and Sapora, 2015; Lenarda and Paggi, 2022). Accordingly, the modulus $E_{poly}$ is given by

$$E_{poly}(t, T) = \frac{a(T)h(t,T)^{-\alpha(T)}}{\Gamma(1 - \alpha(T))} \tag{20}$$

where $a$ and $\alpha$ are two temperature dependent functions, such that $0 < a, \alpha < 1$, and $\Gamma(t)$ is the Euler gamma function

$$\Gamma(t) = \int_0^\infty e^{-x} x^{t-1} \, dx \tag{21}$$

The function $h(t, T)$ is a time history and temperature dependent function, which is used to model the rheologically complex polymeric materials when the time–temperature superposition principle is not applicable. This can be ascribed to the change of polymer microstructure driven by temperature above a threshold. Hence, this history function $h(t, T)$ is equal to the difference between the current time $t$ and $t_0$ corresponding to the microstructure modification.

With regard to the heat conduction, it is assumed that the heat flux across the interface is oriented in the direction orthogonal to the thin polymeric surface. Thus, $q_1 = q_2 = 0$ and $q = q_3$ is expressed as

$$q = \begin{cases} -h_0 \left(1 - \frac{\Delta_n}{\delta_n^c}\right) \langle T \rangle & \text{if } \Delta_n \in J_n \\ 0 & \text{if } \Delta_n \notin J_n \end{cases} \tag{22}$$

where $h_0$ is the thermal conductivity of interface without crack opening, i.e., $\Delta_n = 0$. Note that the heat conductivity is assumed to be a decreasing function of gap opening so that the partial heat transfer in case of damaged interface can be taken into account properly (Sapora and Paggi, 2014).

## 2.3. Moisture diffusion along the polymeric interfaces

Durability tests of photovoltaic laminates, including damp heat test, humidity freeze test, and thermal cycling test, are characterized by time-dependent temperature and moisture conditions in accordance with prescribed ramps inside a climate chamber. Moisture diffusion mainly takes place along the encapsulant polymeric layers between the solar cell and tempered glass or backsheet. Generally, the aim of the numerical method is to predict the moisture content $c(x_1, x_2, x_3, t)$ inside the polymeric layer for each material point and time.

The boundary value problem for moisture diffusion, in which an imposed moisture content $c^*$ is applied to the boundary, can be described as follows

$$\begin{cases} \frac{\partial c}{\partial t}(x_1, x_2, x_3, t) - D\nabla^2 c(x_1, x_2, x_3, t) = 0 & \text{in } \mathcal{B}_{poly} \times [0, t_f] \\ c(x_1, x_2, x_3, 0) = 0 & \text{in } \mathcal{B}_{poly} \\ c(x_1, x_2, x_3, t) = c^* & \text{in } \partial\mathcal{B}_{poly} \times (0, t_f] \end{cases} \tag{23}$$

where $D$ is the moisture diffusion coefficient.

It should be pointed out that the moisture diffusion is characterized by a different time scale from that of the thermo-mechanical problem. The characteristic velocity of moisture diffusion is related to the diffusion coefficient $D$, while that of temperature diffusion is governed by the ratio $k_0/\rho c_p$. Given the characteristic values for polymeric layers, the ratio between these two physical phenomena is

$$\left[k_0 / \left(\rho c_p\right)\right] / D \approx 10^6.$$

Hence, the moisture diffusion is dependent on the coupled thermo-mechanical problem and not viceversa since heat transfer is about six order faster than moisture diffusion. Based on the experimental evidence reported in Kempe (2006), the moisture diffusion coefficient should be considered as temperature and gap dependent based on an Arrhenius type function

$$D = \begin{cases} A \exp\left(-\frac{E_a}{TR}\right), & \text{if } \Delta_n \leq \delta_n^c \\ A \exp\left(-\frac{E_a}{TR}\right) \frac{\Delta_n}{\delta_n^c}, & \text{if } \Delta_n > \delta_n^c \end{cases} \tag{24}$$

For the purpose of accounting for the debonding effect of the encapsulant layer on the moisture diffusion, $D$ is assumed to be a linear increasing function of the interfacial gap $\Delta_n$ when it overcomes the critical value $\delta_n^c$. Given the different time scales of moisture diffusion and heat transfer, a staggered scheme is adopted for the solution of this computational framework, where the diffusion coefficient $D$ is determined by the average temperature and gap displacement at the previous time increment computed from the coupled thermo-mechanical problem.

## 3. Variational form and finite element interpolation

In this section, the derivations for the variational form and finite element formulation of the coupled thermo-mechanical problem with cohesive interface and 3D moisture diffusion are outlined. Section 3.1 introduces the multi-field Hu–Washizu variational principle and discretization for the coupled thermo-mechanical problem, which is particularized for solid shell formulation incorporating the EAS and ANS method to alleviate the locking effects. Subsequently, Section 3.2 presents the consistent linearization of the governing equations for the thermo-mechanical cohesive interface. Finally, the finite element implementation of the 3D moisture diffusion along the encapsulant polymeric layers is detailed in Section 3.3.

### 3.1. Implementation of the coupled thermo-mechanical problem and solid shell formulation

In the following, the variational basis and finite element interpolation of the initial boundary value problem with the coupled thermo-mechanical solid shell formulation are presented. The laminae in photovoltaic modules are usually made of thin-walled structures, including tempered glass, silicon solar cell, and backsheet, and to accurately simulate their mechanical behaviors, a solid shell formulation incorporating the EAS and ANS methods for the alleviation of locking effects is derived from the mixed Hu–Washizu variational principle.

The weak form of energy balance equation in absence of heat sources and dissipative mechanism in the reference configuration is given by

$$\mathcal{R}^T(\mathbf{u}, \tilde{\mathbf{E}}, T, \delta T) = \int_{B_0} \rho_0 c_p \dot{T} \delta T \mathrm{d}\Omega - \int_{B_0} T\mathbf{Z} : \dot{\mathbf{E}} \delta T \ \mathrm{d}\Omega + \int_{B_0} \nabla \cdot \mathbf{Q} \delta T \ \mathrm{d}\Omega = 0, \tag{25}$$

where $\delta T$ is the virtual temperature field. Invoking the Gauss's theorem, the third term relevant to the divergence of heat flux can be reformulated as

$$\int_{B_0} \nabla \cdot \mathbf{Q} \delta T \ \mathrm{d}\Omega = \int_{\partial B_{0,\bar{q}}} Q_N \delta T \ \mathrm{d}\partial\Omega - \int_{B_0} \mathbf{Q} \nabla_\mathbf{X} \delta T \ \mathrm{d}\Omega, \tag{26}$$

where $Q_N = \mathbf{Q} \cdot \mathbf{N}$ denotes the Neumann boundary condition on $\partial B_{0,\bar{q}}$. Subsequently, Eq. (25) can be rewritten as

$$\mathcal{R}^T(\mathbf{u}, \tilde{\mathbf{E}}, T, \delta T) = \int_{B_0} \rho_0 c_p \dot{T} \delta T \ \mathrm{d}\Omega - \int_{B_0} T\mathbf{Z} : \dot{\mathbf{E}} \delta T \ \mathrm{d}\Omega + \int_{\partial B_{0,\bar{q}}} Q_N \delta T \ \mathrm{d}\partial\Omega - \int_{B_0} \mathbf{Q} \nabla_\mathbf{X} \delta T \ \mathrm{d}\Omega = 0. \tag{27}$$

By inserting the Duhamel's law, i.e., simplified Eq. (17) under isotropic assumption, the previous expression can be formulated as

$$\mathcal{R}^T = \int_{B_0} \rho_0 c_p \dot{T} \delta T \ \mathrm{d}\Omega - \int_{B_0} T\mathbf{Z} : \dot{\mathbf{E}} \delta T \ \mathrm{d}\Omega + \int_{\partial B_{0,\bar{q}}} Q_N \delta T \ \mathrm{d}\partial\Omega + \int_{B_0} \left[ \nabla_\mathbf{X} \delta T \right]^\mathrm{T} k_0 \mathbf{G} \nabla_\mathbf{X} T \ \mathrm{d}\Omega = 0, \tag{28}$$

with the internal residual $\mathcal{R}^T_{\mathrm{int}}$ and external counterpart $\mathcal{R}^T_{\mathrm{ext}}$ being identified as

$$\mathcal{R}^T_{\mathrm{int}} = \int_{B_0} \rho_0 c_p \dot{T} \delta T \ \mathrm{d}\Omega - \int_{B_0} T\mathbf{Z} : \dot{\mathbf{E}} \delta T \ \mathrm{d}\Omega + \int_{B_0} \left[ \nabla_\mathbf{X} \delta T \right]^\mathrm{T} k_0 \mathbf{G} \nabla_\mathbf{X} T \ \mathrm{d}\Omega = 0, \tag{29}$$

$$\mathcal{R}^T_{\mathrm{ext}} = \int_{\partial B_{0,\bar{q}}} Q_N \delta T \ \mathrm{d}\partial\Omega. \tag{30}$$

Analogously, the weak form of the linear momentum balance governing can be derived in this procedure. However, low-order shell elements usually suffer from various locking pathologies, such as volumetric locking, Poisson thickness locking, transverse shear locking and so on. To alleviate such deficiencies, the mixed formulation proposed in Gruttmann and Wagner (2006), Klinkel et al. (2006), Simo and Armero (1992) is adopted here, which incorporates the ANS and EAS methods through the enhancement of the displacement derived strain field by several collocation points and a set of incompatible strains. In this three-field Hu–Washizu variational principle, the displacement $\mathbf{u}$, the incompatible strain $\tilde{\mathbf{E}}$, and stress $\mathbf{S}$ are the independent unknown variables for this numerical strategy.

Given the use of EAS method, the strain field can be decomposed into a displacement derived compatible part $\mathbf{E}^u$ and an enhanced incompatible part $\tilde{\mathbf{E}}$ (Bischoff and Ramm, 1997; Hauptmann et al., 2000), i.e., $\mathbf{E} = \mathbf{E}^u + \tilde{\mathbf{E}}$. Accounting for the orthogonality condition between the stress spaces and enhanced strain fields, the stress field can be removed from the subsequent derivations. Hence, the weak form of the linear momentum balance equation can be expressed as

$$\mathcal{R}^u(\mathbf{u}, \tilde{\mathbf{E}}, T, \delta\mathbf{u}) = \int_{B_0} \mathbf{S} : \delta\mathbf{E}^u \ \mathrm{d}\Omega - \int_{B_0} \rho_0 \bar{\boldsymbol{\gamma}} \delta\mathbf{u} \ \mathrm{d}\Omega - \int_{\partial B_{0,\bar{t}}} \hat{\mathbf{t}} \delta\mathbf{u} \ \mathrm{d}\partial\Omega = 0, \tag{31}$$

$$\mathcal{R}^{\tilde{E}}(\mathbf{u}, \tilde{\mathbf{E}}, T, \delta\tilde{\mathbf{E}}) = \int_{B_0} \mathbf{S} : \delta\tilde{\mathbf{E}} \ \mathrm{d}\Omega = \mathcal{R}^{\tilde{E}}_{\mathrm{int}} = 0, \tag{32}$$

where $\mathcal{R}^{\tilde{E}}_{\mathrm{int}}$ represents the internal contribution from the enhanced strain field to the functional. Here the internal residual $\mathcal{R}^u_{\mathrm{int}}$ and external residual $\mathcal{R}^u_{\mathrm{ext}}$ corresponding to the kinematic compatible part can be defined as

$$\mathcal{R}^u_{\mathrm{int}} = \int_{B_0} \mathbf{S} : \delta\mathbf{E}^u \ \mathrm{d}\Omega, \tag{33}$$

ANS for transverse shear locking
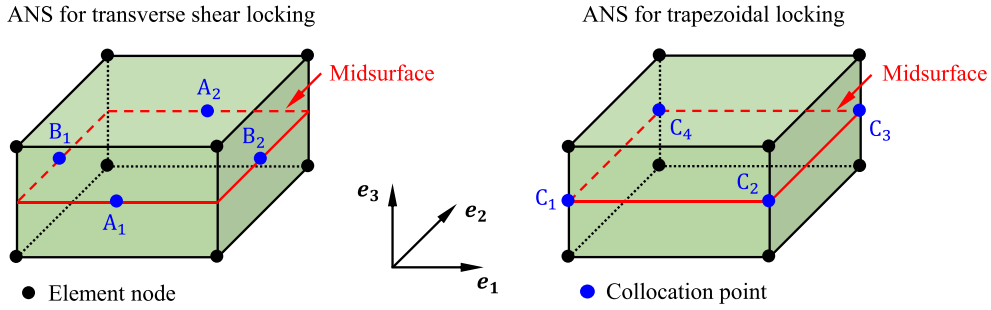
ANS for trapezoidal locking



**Fig. 6.** The position of collocation points in the parametric space for the ANS method.

$$\mathcal{R}^u_{\text{ext}} = \int_{\mathcal{B}_0} \rho_0 \bar{\gamma} \cdot \delta\mathbf{u} \ d\Omega - \int_{\partial\mathcal{B}_{0,\bar{t}}} \hat{\mathbf{t}} \cdot \delta\mathbf{u} \ d\partial\Omega. \tag{34}$$

The initial configuration $\mathcal{B}_0$ is discretized into $n_e$ non-overlapping finite elements, i.e., $\mathcal{B}_0 \approx \bigcup_{e=1}^{n_e} \mathcal{B}_0^{(e)}$. For the thermo-mechanical modeling framework stated above, it is particularized for the so-called solid shell parametrization, which assumes the approximation of vector at any material point in terms of the counterparts on the corresponding top and bottom surfaces of the shell element.

In line with this parametrization, the position vectors and temperature of any material point in the reference and current configurations can be computed as

$$\mathbf{X}(\xi) = \frac{1}{2}\left(1 + \xi^3\right) \mathbf{X}_t(\xi^1, \xi^2) + \frac{1}{2}\left(1 - \xi^3\right) \mathbf{X}_b(\xi^1, \xi^2), \tag{35a}$$

$$\mathbf{x}(\xi) = \frac{1}{2}\left(1 + \xi^3\right) \mathbf{x}_t(\xi^1, \xi^2) + \frac{1}{2}\left(1 - \xi^3\right) \mathbf{x}_b(\xi^1, \xi^2), \tag{35b}$$

where the subscripts $t$ and $b$ stand for the top and bottom surfaces, respectively. The parametric space is given by: $\mathcal{A} := \{\xi = (\xi^1, \xi^2, \xi^3) \in \mathbb{R}^3 | -1 \le \xi^i \le +1; i = 1, 2, 3\}$, where $(\xi^1, \xi^2)$ represent the in-plane directions and $\xi^3$ identifies the thickness direction.

Based on the isoparametric concept, the approximation of position vectors $\mathbf{X}$ and $\mathbf{x}$ are interpolated through standard trilinear shape functions $\mathbf{N}_I$ as follows

$$\mathbf{X} \approx \sum_{I=1}^{n_n} \mathbf{N}_I(\xi)\mathbf{X}_I = \mathbf{N}\widetilde{\mathbf{X}}, \quad \mathbf{x} \approx \sum_{I=1}^{n_n} \mathbf{N}_I(\xi)\mathbf{x}_I = \mathbf{N}\widetilde{\mathbf{x}}, \tag{36}$$

where $\mathbf{X}_I$ and $\mathbf{x}_I$ are the nodal position vectors in the reference and current configurations, respectively, with number of nodes $n_n = 8$, and $\widetilde{\mathbf{X}}$ and $\widetilde{\mathbf{x}}$ are the respective nodal position vectors in the element level. The shape functions $\mathbf{N}_I$ is defined as

$$\mathbf{N}_I = \mathbf{diag}\left[N_I, N_I, N_I\right] \tag{37}$$

where $N_I = \frac{1}{8}\left(1 + \xi_I^1\xi^1\right)\left(1 + \xi_I^2\xi^2\right)\left(1 + \xi_I^3\xi^3\right)$, $I = 1, 2, \ldots, 8$. The interpolation of displacement and temperature fields $(\mathbf{u}, T)$, the variations $(\delta\mathbf{u}, \delta T)$, and the increments $(\varDelta\mathbf{u}, \varDelta T)$ are given by

$$\mathbf{u} \approx \sum_{I=1}^{n_n} \mathbf{N}_I(\xi)\mathbf{d}_I = \mathbf{N}\mathbf{d}, \quad \delta\mathbf{u} \approx \sum_{I=1}^{n_n} \mathbf{N}_I(\xi)\delta\mathbf{d}_I = \mathbf{N}\delta\mathbf{d}, \quad \varDelta\mathbf{u} \approx \sum_{I=1}^{n_n} \mathbf{N}_I(\xi)\varDelta\mathbf{d}_I = \mathbf{N}\varDelta\mathbf{d}, \tag{38}$$

$$T \approx \sum_{I=1}^{n_n} N_I(\xi)T_I = \hat{\mathbf{N}}\hat{T}, \quad \delta T \approx \sum_{I=1}^{n_n} N_I(\xi)\delta T_I = \hat{\mathbf{N}}\delta\hat{T}, \quad \varDelta T \approx \sum_{I=1}^{n_n} N_I(\xi)\varDelta T_I = \hat{\mathbf{N}}\varDelta\hat{T}, \tag{39}$$

where $\mathbf{d}_I$ and $T_I$ represent the nodal displacement and temperature, respectively, and $\mathbf{d}$ and $\hat{T}$ are the corresponding vectors at the element level. The interpolation of the spatial temperature gradient in the reference configuration $\nabla_{\mathbf{X}}T$, its variation $\nabla_{\mathbf{X}}\delta T$ and its increment $\nabla_{\mathbf{X}}\varDelta T$ reads

$$\nabla_{\mathbf{X}}T = \mathbf{G}^{-\mathrm{T}}\nabla_\xi T \approx \mathbf{G}^{-\mathrm{T}}\nabla_\xi\hat{\mathbf{N}}\hat{T}, \quad \nabla_{\mathbf{X}}\delta T \approx \mathbf{G}^{-\mathrm{T}}\nabla_\xi\hat{\mathbf{N}}\delta\hat{T}, \quad \nabla_{\mathbf{X}}\varDelta T \approx \mathbf{G}^{-\mathrm{T}}\nabla_\xi\hat{\mathbf{N}}\varDelta\hat{T}, \tag{40}$$

where $\nabla_\xi$ represents the gradient with respect to the natural coordinates in the curvilinear setting.

The Green–Lagrange strain vector is expressed as $\mathbf{E}^u = \left[E_{11}, 2E_{12}, 2E_{13}, E_{22}, 2E_{23}, E_{33}\right]^{\mathrm{T}}$. To overcome the curvature thickness locking, the ANS method proposed in Betsch and Stein (1995) is adopted to modify the strain component $E_{33}$, which requires four collocation points defined in convective coordinates $\xi_{C_i}$ as $\xi_{C_1} = (-1, -1, 0)$, $\xi_{C_2} = (1, -1, 0)$, $\xi_{C_3} = (1, 1, 0)$, and $\xi_{C_4} = (-1, 1, 0)$, see Fig. 6. Besides, to prevent transverse shear locking, the ANS method proposed in Dvorkin and Bathe (1984) is also adopted in this work. The corresponding collocation points are $\xi_{A_1} = (0, -1, 0)$, $\xi_{A_2} = (0, 1, 0)$, $\xi_{B_1} = (-1, 0, 0)$, and $\xi_{B_2} = (1, 0, 0)$, see Fig. 6.

Accounting for the ANS interpolations, the strain vector is given by

$$
\mathbf{E}^u = \begin{bmatrix}
\frac{1}{2}\left(g_{11} - G_{11}\right) \\
\left(g_{12} - G_{12}\right) \\
\left(1 - \xi^2\right)\left(g_{13}^{A_1} - G_{13}^{A_1}\right) + \left(1 + \xi^2\right)\left(g_{13}^{A_2} - G_{13}^{A_2}\right) \\
\frac{1}{2}\left(g_{22} - G_{22}\right) \\
\left(1 - \xi^1\right)\left(g_{23}^{B_1} - G_{23}^{B_1}\right) + \left(1 + \xi^1\right)\left(g_{23}^{B_2} - G_{23}^{B_2}\right) \\
\sum_{i=1}^{4} \frac{1}{4}\left(1 + \xi_i^1 \xi^1\right)\left(1 + \xi_i^2 \xi^2\right)\frac{1}{2}\left(g_{33}^{C_i} - G_{33}^{C_i}\right)
\end{bmatrix}
\tag{41}
$$

The approximation of strain variation and increment is interpolated by

$$
\delta \mathbf{E}^u \approx \sum_{I=1}^{n_n} \mathbf{B}_I(\xi)\delta \mathbf{d}_I = \mathbf{B}\delta \mathbf{d}, \quad \Delta \mathbf{E}^u \approx \sum_{I=1}^{n_n} \mathbf{B}_I(\xi)\Delta \mathbf{d}_I = \mathbf{B}\Delta \mathbf{d}
\tag{42}
$$

where $\mathbf{B}_I$ is defined as

$$
\mathbf{B}_I = \begin{bmatrix}
N_{I,1}\left(\mathbf{g}_1^{\mathrm{T}}\right) \\
N_{I,1}\left(\mathbf{g}_2^{\mathrm{T}}\right) + N_{I,2}\left(\mathbf{g}_1^{\mathrm{T}}\right) \\
\left(1 - \xi^2\right)\left(N_{I,1}^{A_1}\left(\mathbf{g}_3^{A_1}\right)^{\mathrm{T}} + N_{I,3}^{A_1}\left(\mathbf{g}_1^{A_1}\right)^{\mathrm{T}}\right) + \left(1 + \xi^2\right)\left(N_{I,1}^{A_2}\left(\mathbf{g}_3^{A_2}\right)^{\mathrm{T}} + N_{I,3}^{A_2}\left(\mathbf{g}_1^{A_2}\right)^{\mathrm{T}}\right) \\
N_{I,2}\left(\mathbf{g}_2^{\mathrm{T}}\right) \\
\left(1 - \xi^1\right)\left(N_{I,2}^{B_1}\left(\mathbf{g}_3^{B_1}\right)^{\mathrm{T}} + N_{I,3}^{B_1}\left(\mathbf{g}_2^{B_1}\right)^{\mathrm{T}}\right) + \left(1 + \xi^1\right)\left(N_{I,2}^{B_2}\left(\mathbf{g}_3^{B_2}\right)^{\mathrm{T}} + N_{I,3}^{B_2}\left(\mathbf{g}_2^{B_2}\right)^{\mathrm{T}}\right) \\
\sum_{i=1}^{4} \frac{1}{4}\left(1 + \xi_i^1 \xi^1\right)\left(1 + \xi_i^2 \xi^2\right) N_{I,3}\left(\mathbf{g}_3^{i}\right)^{\mathrm{T}}
\end{bmatrix}
\tag{43}
$$

Similarly, the interpolation of enhanced incompatible strain field $\tilde{\mathbf{E}}$, its variation $\delta\tilde{\mathbf{E}}$ and its increment $\Delta\tilde{\mathbf{E}}$ take the form of

$$
\tilde{\mathbf{E}} \approx \mathbf{M}(\xi)\boldsymbol{\varsigma}, \quad \delta\tilde{\mathbf{E}} \approx \mathbf{M}(\xi)\delta\boldsymbol{\varsigma}, \quad \Delta\tilde{\mathbf{E}} \approx \mathbf{M}(\xi)\Delta\boldsymbol{\varsigma},
\tag{44}
$$

where $\boldsymbol{\varsigma}$ is the enhancing modes vector to prevent locking pathologies as pointed out in Klinkel et al. (2006), Vu-Quoc and Tan (2003), and $\mathbf{M}$ denotes the interpolation matrix of incompatible strain (Simo et al., 1990), which is given by

$$
\mathbf{M}(\xi) = \left[\frac{\det \mathbf{J}_0}{\det \mathbf{J}}\right]\mathbf{T}_0^{-\mathrm{T}}\tilde{\mathbf{M}}(\xi)
\tag{45}
$$

where $\mathbf{J} = \left[\mathbf{G}_1, \mathbf{G}_2, \mathbf{G}_3\right]^{\mathrm{T}}$, $\mathbf{J}_0$ is its evaluation at the element center $\left(\xi^1 = 0, \xi^2 = 0, \xi^3 = 0\right)$, and the transformation matrix $\mathbf{T}_0$ takes the form

$$
\mathbf{T}_0 = \begin{bmatrix}
J_{11_0}^2 & J_{21_0}^2 & J_{31_0}^2 & 2J_{11_0}J_{21_0} & 2J_{11_0}J_{31_0} & 2J_{21_0}J_{31_0} \\
J_{12_0}^2 & J_{22_0}^2 & J_{32_0}^2 & 2J_{12_0}J_{22_0} & 2J_{12_0}J_{32_0} & 2J_{22_0}J_{32_0} \\
J_{13_0}^2 & J_{23_0}^2 & J_{33_0}^2 & 2J_{13_0}J_{23_0} & 2J_{13_0}J_{33_0} & 2J_{23_0}J_{33_0} \\
J_{11_0}J_{12_0} & J_{21_0}J_{22_0} & J_{31_0}J_{32_0} & J_{11_0}J_{22_0} + J_{21_0}J_{12_0} & J_{11_0}J_{32_0} + J_{31_0}J_{12_0} & J_{21_0}J_{32_0} + J_{31_0}J_{22_0} \\
J_{11_0}J_{13_0} & J_{21_0}J_{23_0} & J_{31_0}J_{33_0} & J_{11_0}J_{23_0} + J_{21_0}J_{13_0} & J_{11_0}J_{33_0} + J_{31_0}J_{13_0} & J_{21_0}J_{33_0} + J_{31_0}J_{23_0} \\
J_{12_0}J_{13_0} & J_{22_0}J_{23_0} & J_{32_0}J_{33_0} & J_{12_0}J_{23_0} + J_{22}J_{13_0} & J_{12_0}J_{33_0} + J_{32_0}J_{13_0} & J_{22_0}J_{33_0} + J_{32_0}J_{23_0}
\end{bmatrix}.
\tag{46}
$$

where $J_{IJ_0}$ in the transformation matrix $\mathbf{T}_0$ are the components of $\mathbf{J}_0$. To alleviate the membrane, volumetric and Poisson thickness locking effects, the interpolation matrix $\tilde{\mathbf{M}}(\xi)$ of the enhancing modes defined in the parametric space $\boldsymbol{\xi} = \{\xi^1, \xi^2, \xi^3\}$ reads

$$
\tilde{\mathbf{M}} = \begin{bmatrix}
\xi^1 & 0 & 0 & 0 & \xi^1\xi^2 & 0 & 0 & 0 & 0 & 0 & 0 \\
0 & 0 & \xi^1 & \xi^2 & 0 & 0 & \xi^1\xi^2 & 0 & 0 & 0 & 0 \\
0 & 0 & 0 & 0 & 0 & 0 & 0 & 0 & 0 & 0 & 0 \\
0 & \xi^2 & 0 & 0 & 0 & \xi^1\xi^2 & 0 & 0 & 0 & 0 & 0 \\
0 & 0 & 0 & 0 & 0 & 0 & 0 & 0 & 0 & 0 & 0 \\
0 & 0 & 0 & 0 & 0 & 0 & 0 & 1 & \xi^1 & \xi^2 & \xi^1\xi^2
\end{bmatrix}.
\tag{47}
$$

By inserting the interpolation formulae, the discrete forms of internal energy balance residual Eq. (29) is given by

$$
\hat{\mathcal{R}}_{\text{int}}^T(\mathbf{d}, \boldsymbol{\varsigma}, \hat{\boldsymbol{T}}, \delta\hat{\boldsymbol{T}}) = \delta\hat{\boldsymbol{T}}^{\mathrm{T}}\left[\int_{B_0} \hat{\mathbf{N}}^{\mathrm{T}}\rho_0 c_p \dot{T}\, \mathrm{d}\Omega - \int_{B_0} \hat{\mathbf{N}}^{\mathrm{T}}\left(\mathbf{Z}^{\mathrm{T}}\dot{\mathbf{E}}\right)T\, \mathrm{d}\Omega + \int_{B_0} k_0 \mathbf{B}_T^{\mathrm{T}}\mathbf{G}\nabla_{\mathbf{X}}T\, \mathrm{d}\Omega\right],
\tag{48}
$$

where $\mathbf{B}_T$ is the interpolation operator for the temperature gradient.

The discrete internal residual terms with regard to the kinematic compatible part, Eq. (33), and enhanced strain field, Eq. (32), can be expressed as

$$
\hat{\mathcal{R}}_{\text{int}}^u(\mathbf{d}, \boldsymbol{\varsigma}, \hat{\boldsymbol{T}}, \delta\mathbf{d}) = \delta\mathbf{d}^{\mathrm{T}}\left[\int_{B_0} \mathbf{B}^{\mathrm{T}}\mathbf{S}\, \mathrm{d}\Omega\right],
\tag{49}
$$

$$\hat{\mathcal{R}}_{\text{int}}^{\hat{E}}(\mathbf{d}, \varsigma, \hat{\boldsymbol{T}}, \delta\varsigma) = \delta\varsigma^{\text{T}} \left[ \int_{B_0} \mathbf{M}^{\text{T}} \mathbf{S} \, d\Omega \right]. \tag{50}$$

For subsequent developments, the residual vectors associated with the displacement field, the incompatible strain field, and the temperature field, respectively, are defined as

$$\mathbf{R}_{\text{int}}^{T} = \int_{B_0} \hat{\mathbf{N}}^{\text{T}} \rho_0 c_p \dot{T} d\Omega - \int_{B_0} \hat{\mathbf{N}}^{\text{T}} \left( \mathbf{Z}^{\text{T}} \dot{\mathbf{E}} \right) T d\Omega + \int_{B_0} k_0 \mathbf{B}_T^{\text{T}} \mathbf{G} \nabla_{\mathbf{X}} T \, d\Omega, \tag{51a}$$

$$\mathbf{R}_{\text{int}}^{d} = \int_{B_0} \mathbf{B}^{\text{T}} \mathbf{S} \, d\Omega, \tag{51b}$$

$$\mathbf{R}_{\text{int}}^{\varsigma} = \int_{B_0} \mathbf{M}^{\text{T}} \mathbf{S} \, d\Omega. \tag{51c}$$

To solve the set of nonlinear residual equations, the iterative scheme is adopted for the multi-field coupled thermo-mechanical problem, and the consistent linearization of the system derived from the concept of Gateaux directional derivative in matrix form can be expressed as

$$\begin{bmatrix} \mathbf{k}_{dd} & \mathbf{k}_{d\varsigma} & \mathbf{k}_{dT} \\ \mathbf{k}_{\varsigma d} & \mathbf{k}_{\varsigma\varsigma} & \mathbf{k}_{\varsigma T} \\ \mathbf{k}_{Td} & \mathbf{k}_{T\varsigma} & \mathbf{k}_{TT} \end{bmatrix} \begin{bmatrix} \Delta\mathbf{d} \\ \Delta\varsigma \\ \Delta\hat{T} \end{bmatrix} = \begin{bmatrix} \mathbf{R}_{\text{ext}}^{d} \\ \mathbf{0} \\ \mathbf{R}_{\text{ext}}^{T} \end{bmatrix} - \begin{bmatrix} \mathbf{R}_{\text{int}}^{d} \\ \mathbf{R}_{\text{int}}^{\varsigma} \\ \mathbf{R}_{\text{int}}^{T} \end{bmatrix} \tag{52}$$

where $\mathbf{k}_{ab}$ with $\{a, b\} = \{d, \varsigma, T\}$ are different element tangent operators.

Firstly the tangent operators derived from the linearized residual form of Eq. (51a) with respect to the energy balance reads

$$\mathbf{k}_{TT} = \int_{B_0} \hat{\mathbf{N}}^{\text{T}} \frac{\rho_0 c_p}{\Delta t} \hat{\mathbf{N}} \, d\Omega - \int_{B_0} \hat{\mathbf{N}}^{\text{T}} \left( \mathbf{Z}^{\text{T}} \dot{\mathbf{E}} \right) \hat{\mathbf{N}} \, d\Omega + \int_{B_0} k_0 \mathbf{B}_T^{\text{T}} \mathbf{G} \mathbf{B}_T \, d\Omega, \tag{53a}$$

$$\mathbf{k}_{T\varsigma} = - \int_{B_0} \hat{\mathbf{N}}^{\text{T}} \frac{T}{\Delta t} \mathbf{Z}^{\text{T}} \mathbf{M} \, d\Omega, \tag{53b}$$

$$\mathbf{k}_{Td} = - \int_{B_0} \hat{\mathbf{N}}^{\text{T}} \frac{T}{\Delta t} \mathbf{Z}^{\text{T}} \mathbf{B} \, d\Omega, \tag{53c}$$

where $\Delta t$ is the time increment.

Analogously, the tangent operators obtained from linearization of the residual equation Eq. (51b) with respect to the displacement field is given by

$$\mathbf{k}_{dT} = \int_{B_0} \mathbf{B}^{\text{T}} \mathbf{Z} \hat{\mathbf{N}} \, d\Omega \tag{54a}$$

$$\mathbf{k}_{d\varsigma} = \int_{B_0} \mathbf{B}^{\text{T}} \mathbb{C} \mathbf{M} \, d\Omega, \tag{54b}$$

$$\mathbf{k}_{dd} = \int_{B_0} \left( \mathbf{B}^{\text{T}} \mathbb{C} \mathbf{B} + \mathbf{Q} \right) \, d\Omega. \tag{54c}$$

where $\mathbf{Q}$ represents the geometrical nonlinearity, which is defined as

$$\mathbf{Q} = \frac{\partial \mathbf{B}(\mathbf{d})^{\text{T}}}{\partial \mathbf{d}} \mathbf{S} = \begin{bmatrix} \mathbf{Q}_{11} & \mathbf{Q}_{12} & \cdots & \mathbf{Q}_{18} \\ \mathbf{Q}_{21} & \mathbf{Q}_{22} & \cdots & \mathbf{Q}_{28} \\ \vdots & \vdots & \ddots & \vdots \\ \mathbf{Q}_{81} & \mathbf{Q}_{82} & \cdots & \mathbf{Q}_{88} \end{bmatrix} \tag{55}$$

where $\mathbf{Q}_{IJ}$ is defined as $\mathbf{Q}_{IJ} = \text{diag} \left[ Q_{IJ}, Q_{IJ}, Q_{IJ} \right]$ for the combination of node $I$ and $J$, and the scalar $Q_{IJ}$ reads

$$Q_{IJ} = \mathbf{S}^{\text{T}} \begin{bmatrix} N_{I,1} N_{J,1} \\ N_{I,1} N_{J,2} + N_{I,2} N_{J,1} \\ \left( 1 - \xi^2 \right) \left( N_{I,1}^{\text{A}_1} N_{J,3}^{\text{A}_1} + N_{I,3}^{\text{A}_1} N_{J,1}^{\text{A}_1} \right) + \left( 1 + \xi^2 \right) \left( N_{I,1}^{\text{A}_2} N_{J,3}^{\text{A}_2} + N_{I,3}^{\text{A}_2} N_{J,1}^{\text{A}_2} \right) \\ N_{I,2} N_{J,2} \\ \left( 1 - \xi^1 \right) \left( N_{I,2}^{\text{B}_1} N_{J,3}^{\text{B}_1} + N_{I,3}^{\text{B}_1} N_{J,2}^{\text{B}_1} \right) + \left( 1 + \xi^1 \right) \left( N_{I,2}^{\text{B}_2} N_{J,3}^{\text{B}_2} + N_{I,3}^{\text{B}_2} N_{J,2}^{\text{B}_2} \right) \\ \sum_{i=1}^{4} \frac{1}{4} \left( 1 + \xi_i^1 \xi^1 \right) \left( 1 + \xi_i^2 \xi^2 \right) N_{I,3} N_{J,3} \end{bmatrix} \tag{56}$$

where $\mathbf{S}$ is the approximate stress field in matrix form as $\mathbf{S} = \left[ \mathbf{S}^{11}, \mathbf{S}^{12}, \mathbf{S}^{13}, \mathbf{S}^{22}, \mathbf{S}^{23}, \mathbf{S}^{33} \right]^{\text{T}}$.

Similarly, the tangent operators derived from Eq. (51c) with respect to the incompatible strain field take the form

$$\mathbf{k}_{\varsigma T} = \int_{B_0} \mathbf{M}^{\text{T}} \mathbf{Z} \hat{\mathbf{N}} \, d\Omega, \tag{57a}$$
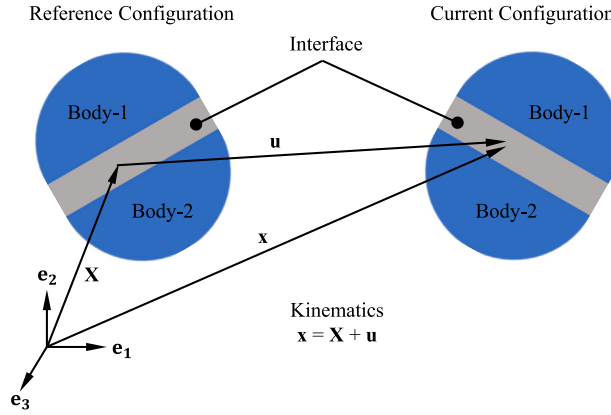
**Fig. 7.** Sketch of the interface between the two bodies during the deformation process.

$$\mathbf{k}_{\varsigma d} = \int_{B_0} \mathbf{M}^{\mathrm{T}} \mathbb{C} \mathbf{B} \, \mathrm{d}\Omega, \tag{57b}$$

$$\mathbf{k}_{\varsigma\varsigma} = \int_{B_0} \mathbf{M}^{\mathrm{T}} \mathbb{C} \mathbf{M} \, \mathrm{d}\Omega, \tag{57c}$$

Since inter-element continuity is not required (Reinoso and Blázquez, 2016), the consistent linearization with respect to the incompatible strain field can be condensed out in the element level, and the condensed system of equations are given by

$$\begin{bmatrix} \mathbf{k}_{dd}^* & \mathbf{k}_{dT}^* \\ \mathbf{k}_{Td}^* & \mathbf{k}_{TT}^* \end{bmatrix} \begin{bmatrix} \Delta\mathbf{d} \\ \Delta T \end{bmatrix} = \begin{bmatrix} \mathbf{R}_{\mathrm{ext}}^d \\ \mathbf{R}_{\mathrm{ext}}^T \end{bmatrix} - \begin{bmatrix} \mathbf{R}_{\mathrm{int}}^{d*} \\ \mathbf{R}_{\mathrm{int}}^{T*} \end{bmatrix} \tag{58}$$

where the element stiffness contributions are

$$\mathbf{k}_{dd}^* = \mathbf{k}_{dd} - \mathbf{k}_{d\varsigma} \mathbf{k}_{\varsigma\varsigma}^{-1} \mathbf{k}_{\varsigma d}, \quad \mathbf{k}_{dT}^* = \mathbf{k}_{dT} - \mathbf{k}_{d\varsigma} \mathbf{k}_{\varsigma\varsigma}^{-1} \mathbf{k}_{\varsigma T}, \tag{59a}$$

$$\mathbf{k}_{Td}^* = \mathbf{k}_{Td} - \mathbf{k}_{T\varsigma} \mathbf{k}_{\varsigma\varsigma}^{-1} \mathbf{k}_{\varsigma d}, \quad \mathbf{k}_{TT}^* = \mathbf{k}_{TT} - \mathbf{k}_{T\varsigma} \mathbf{k}_{\varsigma\varsigma}^{-1} \mathbf{k}_{\varsigma T}, \tag{59b}$$

and the condensed element internal residual vectors render

$$\mathbf{R}_{\mathrm{int}}^{d*} = \mathbf{R}_{\mathrm{int}}^d - \mathbf{k}_{d\varsigma} \mathbf{k}_{\varsigma\varsigma}^{-1} \mathbf{R}_{\mathrm{int}}^{\varsigma}, \tag{60a}$$

$$\mathbf{R}_{\mathrm{int}}^{T*} = \mathbf{R}_{\mathrm{int}}^T - \mathbf{k}_{T\varsigma} \mathbf{k}_{\varsigma\varsigma}^{-1} \mathbf{R}_{\mathrm{int}}^{\varsigma}. \tag{60b}$$

### 3.2. Finite element implementation of cohesive interface

In the reference configuration for finite deformation setting, consider two deformable bodies $\mathcal{B}_0^{(1)} \subset \mathbb{R}^3$ and $\mathcal{B}_0^{(2)} \subset \mathbb{R}^3$ (identified as Body-1 and Body-2 in Fig. 7). The interface contribution of cohesive traction $\bar{\sigma} = (\sigma, \tau_t, \tau_s)$ and heat flux $\bar{q}$ to the Principle of Virtual Work of the whole mechanical system can be expressed as

$$\Pi_{\mathrm{int}} = \int_{\Gamma_{\mathrm{int}}} \mathbf{g}_{\mathrm{loc}}^{\mathrm{T}} \cdot \mathbf{T} \, \mathrm{d}\partial\Omega \tag{61}$$

where $\mathbf{g}_{\mathrm{loc}} = (\Delta_n, \Delta_s, \Delta_t, \Delta_T)^{\mathrm{T}}$ is the local gap vector including both mechanical and thermal gaps, and $\mathbf{T} = (\sigma, \tau_t, \tau_s, \bar{q})$ is the traction vector conjugate to the gap vector. Note that the traction vector vanishes when the interface is undergoing rigid body motions owning to the frame indifference of this formulation. The variational form of interface contribution is given by

$$\delta\Pi_{\mathrm{int}}(\mathbf{g}_{\mathrm{loc}}) = \int_{\Gamma_{\mathrm{int}}} \left( \frac{\partial \mathbf{g}_{\mathrm{loc}}}{\partial \hat{\mathbf{u}}} \delta\hat{\mathbf{u}} \right)^{\mathrm{T}} \mathbf{T} \, \mathrm{d}\partial\Omega = \delta\hat{\mathbf{u}}^{\mathrm{T}} \int_{\Gamma_{\mathrm{int}}} \left( \frac{\partial \mathbf{g}_{\mathrm{loc}}}{\partial \hat{\mathbf{u}}} \right)^{\mathrm{T}} \mathbf{T} \, \mathrm{d}\partial\Omega \tag{62}$$

where $\hat{\mathbf{u}} = (\mathbf{u}, T)^{\mathrm{T}}$ is the generalized field vector.

To account for the rotations of configuration, a middle plane of the interface by averaging the position and displacement vector of the upper and lower faces is defined. Hence, the position vector on the middle surface $\bar{\mathbf{x}}$ and $\bar{\mathbf{X}}$ can be determined by multiplying the position vector with an averaging operator $\mathbf{M}^{cz}$,

$$\bar{\mathbf{x}} = \mathbf{M}^{cz} \mathbf{x}, \quad \bar{\mathbf{X}} = \mathbf{M}^{cz} \mathbf{X} \tag{63}$$
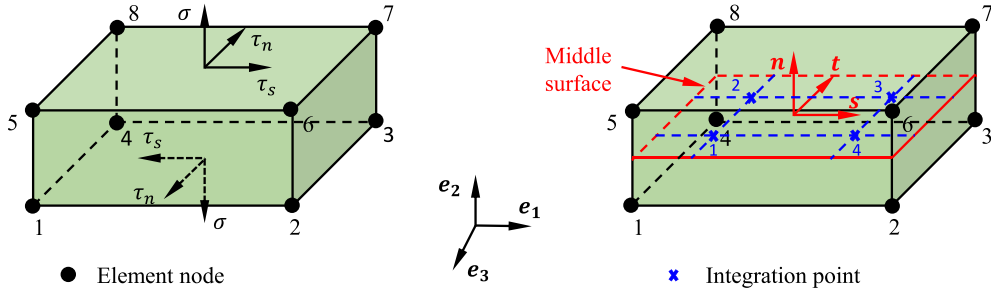
**Fig. 8.** Sketch of the three-dimensional interface finite element.



**Fig. 9.** The sketch of double-glass structure in the damp heat test.

where the matrix $\mathbf{M}^{cz}$ is defined as $\mathbf{M}^{cz} = \frac{1}{2}(\mathcal{I}_{12}, \mathcal{I}_{12})$ with $\mathcal{I}_{12}$ identified as $12 \times 12$ identity matrix.

In line with derivations proposed in Reinoso et al. (2012), the convective shear vector $\mathbf{s}$, tangential vector $\mathbf{t}$ and normal vector $\mathbf{n}$ to the middle surface, see Fig. 8, are defined via the differentiation of average position vector in the current configuration with respect to the natural coordinates $\xi$ and $\eta$, and given by

$$\mathbf{s} = \frac{\partial \bar{\mathbf{x}}}{\partial \xi}, \quad \mathbf{t} = \frac{\partial \bar{\mathbf{x}}}{\partial \eta}, \quad \mathbf{n} = \mathbf{s} \times \mathbf{t}. \tag{64}$$

The gap vector $\mathbf{g}$ can be determined by multiplying the nodal displacement vector of the interface element with an appropriate operator $\mathbf{L}^{cz} = (-\mathcal{I}_{16}, \mathcal{I}_{16})$ with $\mathcal{I}_{16}$ identified as $16 \times 16$ identity matrix, which provides the difference between the bottom and upper surface displacements, and its expression is given by

$$\mathbf{g} = \mathbf{N}^{cz} \mathbf{L}^{cz} \hat{\mathbf{d}} \tag{65}$$

where $\hat{\mathbf{d}}$ is the vector collecting the degrees of freedom in the element level, and $\mathbf{N}^{cz}$ is the interpolation matrix of interface, which reads

$$\mathbf{N}^{cz} = \left[ N_1^{cz} \mathcal{I}_4, N_2^{cz} \mathcal{I}_4, N_3^{cz} \mathcal{I}_4, N_4^{cz} \mathcal{I}_4 \right], \tag{66}$$

where $N_1^{cz} = \frac{1}{4}(1-\xi)(1-\eta)$, $N_2^{cz} = \frac{1}{4}(1+\xi)(1-\eta)$, $N_3^{cz} = \frac{1}{4}(1+\xi)(1+\eta)$ and $N_4^{cz} = \frac{1}{4}(1-\xi)(1+\eta)$, and $\mathcal{I}_4$ is the $4 \times 4$ identity matrix.

To define the traction–separation law in the local frame, the local gap vector needs to be computed by multiplying the counterpart in the global frame with a rotation matrix operator

$$\mathbf{g}_{\text{loc}} = \mathbf{R}_{cz} \mathbf{g} = \mathbf{R}_{cz} \mathbf{N}^{cz} \mathbf{L}^{cz} \hat{\mathbf{d}}, \tag{67}$$

and the rotation matrix $\mathbf{R}_{cz}$ reads

$$\mathbf{R}_{cz} = \begin{bmatrix} s_x & s_y & s_z & 0 \\ t_x & t_y & t_z & 0 \\ n_x & n_y & n_z & 0 \\ 0 & 0 & 0 & 1 \end{bmatrix} \tag{68}$$

where its coefficients are all components of the convective vectors defined in Eq. (64).

Recalling the derivation of Eq. (62), the partial derivative of the local gap vector with respect to nodal displacements takes the form

$$\frac{\partial \mathbf{g}_{\text{loc}}}{\partial \hat{\mathbf{u}}} \approx \frac{\partial \mathbf{g}_{\text{loc}}}{\partial \hat{\mathbf{d}}} = \mathbf{R}_{cz} \mathbf{N}^{cz} \mathbf{L}^{cz} + \frac{\partial \mathbf{R}_{cz}}{\partial \hat{\mathbf{d}}} \mathbf{N}^{cz} \mathbf{L}^{cz} \hat{\mathbf{d}} = \mathbf{R}_{cz} \mathbf{B}_{cz} + \frac{\partial \mathbf{R}_{cz}}{\partial \hat{\mathbf{d}}} \mathbf{B}_{cz} \hat{\mathbf{d}}. \tag{69}$$

where $\mathbf{B}_{cz} = \mathbf{N}^{cz} \mathbf{L}^{cz}$ is introduced to simplify the equation. By inserting Eq. (69) into Eq. (61), where $\mathbf{u}$ is replaced by the nodal vector $\hat{\mathbf{d}}$, the general variational form of interface element formulation is given by

$$\delta \Pi_{\text{int}} = \delta \hat{\mathbf{d}}^{\text{T}} \int_{\text{int}} \left( \mathbf{R}_{cz} \mathbf{B}_{cz} + \frac{\partial \mathbf{R}_{cz}}{\partial \hat{\mathbf{d}}} \mathbf{B}_{cz} \hat{\mathbf{d}} \right)^{\text{T}} \mathbf{T} \, \mathrm{d}\partial\Omega = \delta \hat{\mathbf{d}}^{\text{T}} \mathbf{f}_{\text{int}} \tag{70}$$

(a) 100 h     (b) 300 h     (c) 400 h

(d) 500 h     (e) 600 h     (f) 700 h
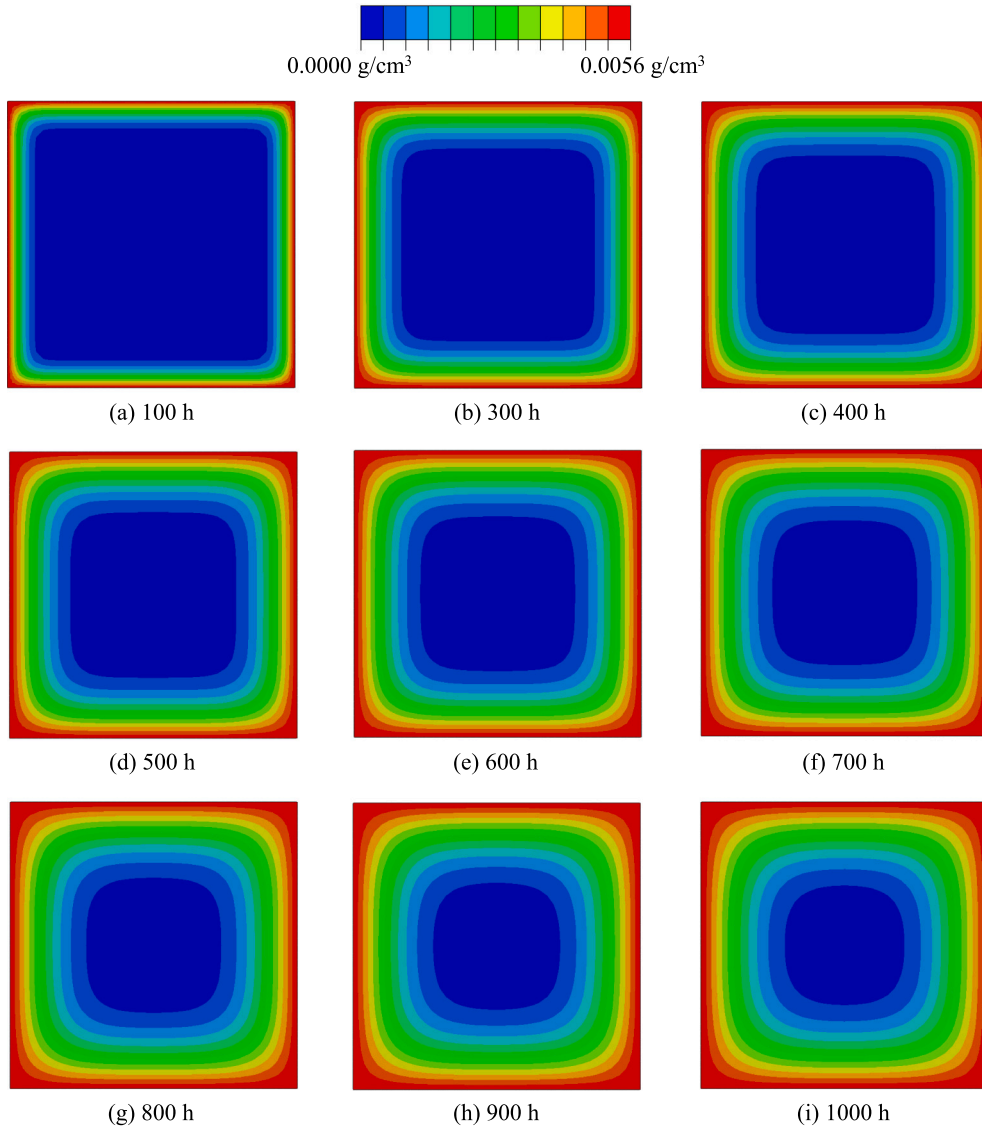
(g) 800 h     (h) 900 h     (i) 1000 h

**Fig. 10.** The contour plot of moisture diffusion along the EVA layer inside the double-glass laminate during the damp heat simulation.

where the vector $\delta\hat{\mathbf{d}}$ represents the admissible virtual nodal vector, and $\mathbf{f}_{\text{int}}$ is the internal force vector of interface at the element level. The consistent linearization for the interface finite element formulation at the $(k+1)th$ iteration is given by

$$\mathbf{K}^{e,k}\Delta\hat{\mathbf{d}}^{k+1} = -\mathbf{f}_{\text{int}}^{k} \tag{71a}$$

$$\hat{\mathbf{d}}^{k+1} = \hat{\mathbf{d}}^{k} + \Delta\hat{\mathbf{d}}^{k+1} \tag{71b}$$

where $\mathbf{K}^{e,k} = \dfrac{\partial\mathbf{f}_{\text{int}}}{\partial\hat{\mathbf{d}}}$ is the element stiffness evaluated at the $(k)th$ iteration, which reads

$$\mathbf{K}^{e} = \int_{\Gamma_{\text{int}}} \left[ 2\mathbf{B}_{cz}^{\mathrm{T}} \frac{\partial\mathbf{R}_{cz}^{\mathrm{T}}}{\partial\hat{\mathbf{d}}}\mathbf{T} + \left( \mathbf{B}_{cz}^{\mathrm{T}}\mathbf{R}_{cz}^{\mathrm{T}} + \hat{\mathbf{d}}^{\mathrm{T}}\mathbf{B}_{cz}^{\mathrm{T}} \frac{\partial\mathbf{R}_{cz}^{\mathrm{T}}}{\partial\hat{\mathbf{d}}} \right) \frac{\partial\mathbf{T}}{\partial\hat{\mathbf{d}}} \right] \, \mathrm{d}\partial\Omega. \tag{72}$$

It should be pointed out that the second derivative of the rotation matrix with respect to the nodal vector is omitted for convenience in the formulation (Reinoso and Paggi, 2014). The derivative of cohesive traction vector can be derived by chain rule as follows,

$$\frac{\partial\mathbf{T}}{\partial\hat{\mathbf{d}}} = \frac{\partial\mathbf{T}}{\partial\mathbf{g}_{\text{loc}}} \frac{\partial\mathbf{g}_{\text{loc}}}{\partial\hat{\mathbf{d}}} = \mathbf{C}_{cz}\mathbf{R}_{cz}\mathbf{B}_{cz} + \frac{\partial\mathbf{R}_{cz}}{\partial\hat{\mathbf{d}}}\mathbf{B}_{cz}\hat{\mathbf{d}} \tag{73}$$

where $\mathbf{C}_{cz}$ is the material tangent stiffness of the interface. In small displacement setting, the second term of Eq. (73) with respect to the partial derivative of rotation matrix can be neglected. After substituting Eq. (73) into Eq. (72), the final element stiffness
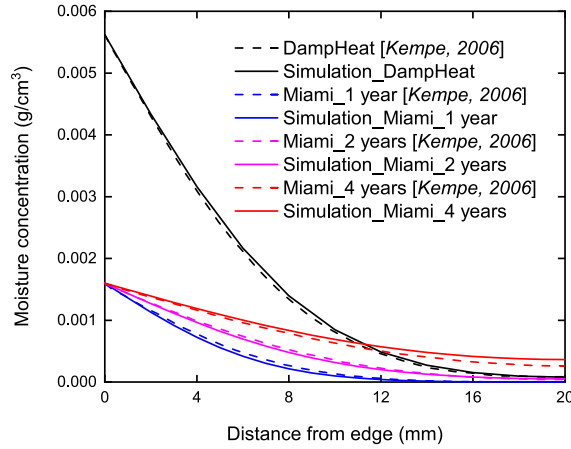
**Fig. 11.** The comparison of moisture concentration vs. distance from the edge of laminate curves between diffusion simulation and damp heat test after 1000 h as well as experimental data in Miami.
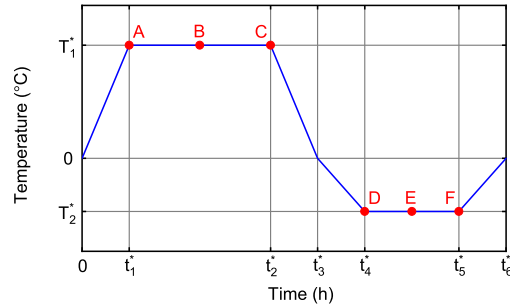


**Fig. 12.** Temperature profile imposed inside the chamber during the humidity freeze test.

matrix form of interface can be expressed as

$$\mathbf{K}^{e} = \int_{\Gamma_{\text{int}}} \mathbf{B}_{cz}^{\mathrm{T}} \mathbf{R}_{cz}^{\mathrm{T}} \mathbf{C}_{cz} \mathbf{R}_{cz} \mathbf{B}_{cz} \ \mathrm{d}\partial\Omega. \tag{74}$$

### 3.3. Finite element implementation of 3D moisture diffusion

The weak form and finite element discretization of 3D moisture diffusion along the polymeric encapsulant layer will be presented in this section. Since a staggered scheme is adopted for the solution of hygro-thermo-visco-elastic problem, the finite element mesh for moisture diffusion can be different from that of thermo-mechanical model. Hence, an appropriate interpolation scheme is required to project the nodal temperatures from the thermo-mechanical problem to the nodes of mesh for moisture diffusion to determine the diffusion coefficients as stated in Eq. (24). In the sequel, the finite element mesh for moisture diffusion coincident with the discretization for the thermo-mechanical interface of encapsulant layers is adopted for convenience, but without any loss of generality.

By multiplying Eq. (23) with a test function $\delta c(\mathbf{X}, t)$, the weak form for moisture diffusion after integration by parts can be constructed as follows

$$\int_{B_0} D\nabla_{\mathbf{X}} c \cdot \nabla_{\mathbf{X}} \delta c \ \mathrm{d}\Omega + \int_{B_0} \delta c \frac{\partial c}{\partial t} \ \mathrm{d}\Omega = 0. \tag{75}$$

The interpolation of moisture concentration and its variation in a generic material point $\mathbf{X}$ and at the time point $t$ is given by
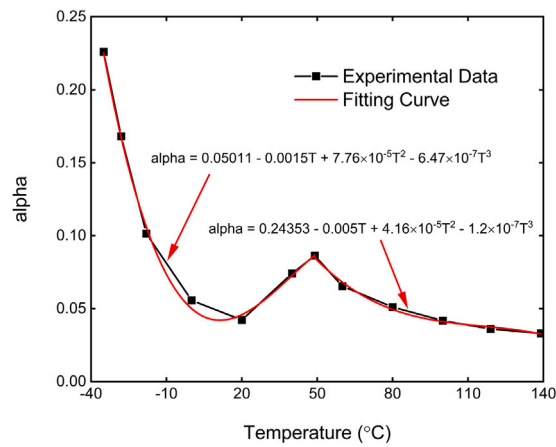
$$c(\mathbf{X}, t) \approx \sum_{I=1}^{n_n} N_I(\boldsymbol{\xi}) c_I = \mathbf{N}_c \tilde{\mathbf{c}}, \quad \delta c(\mathbf{X}, t) \approx \sum_{I=1}^{n_n} N_I(\boldsymbol{\xi}) \delta c_I = \mathbf{N}_c \delta \tilde{\mathbf{c}}, \tag{76}$$
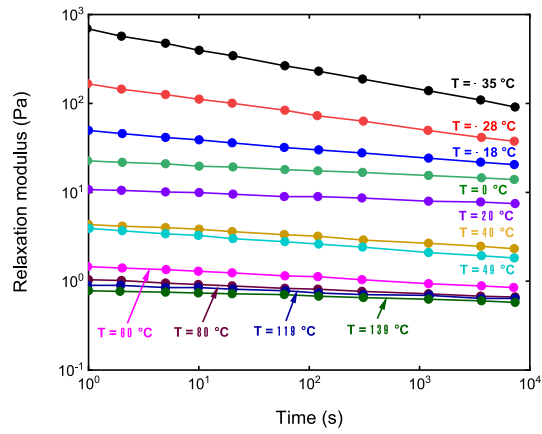
(a)
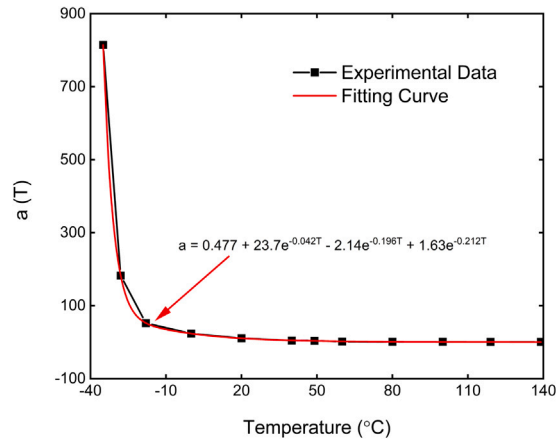


(b)



(c)

**Fig. 13.** (a) Relaxation modulus of EVA vs. time curves at different temperatures, (b) temperature dependent fractional calculus coefficient $a(T)$, (c) temperature dependent exponent $\alpha(T)$.
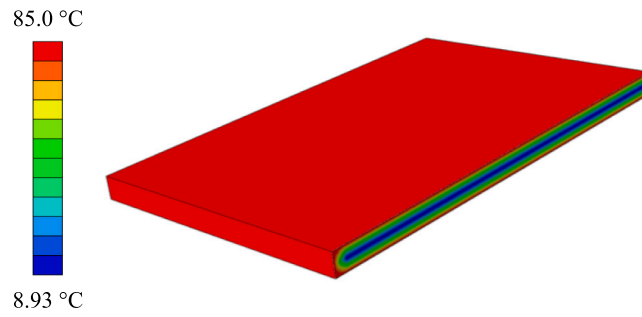*Source:* Adapted from Paggi and Sapora (2015).

**Fig. 14.** The temperature contour plot of the cross section of the double glass laminate at time point A in the first cycle during humidity freeze simulation.
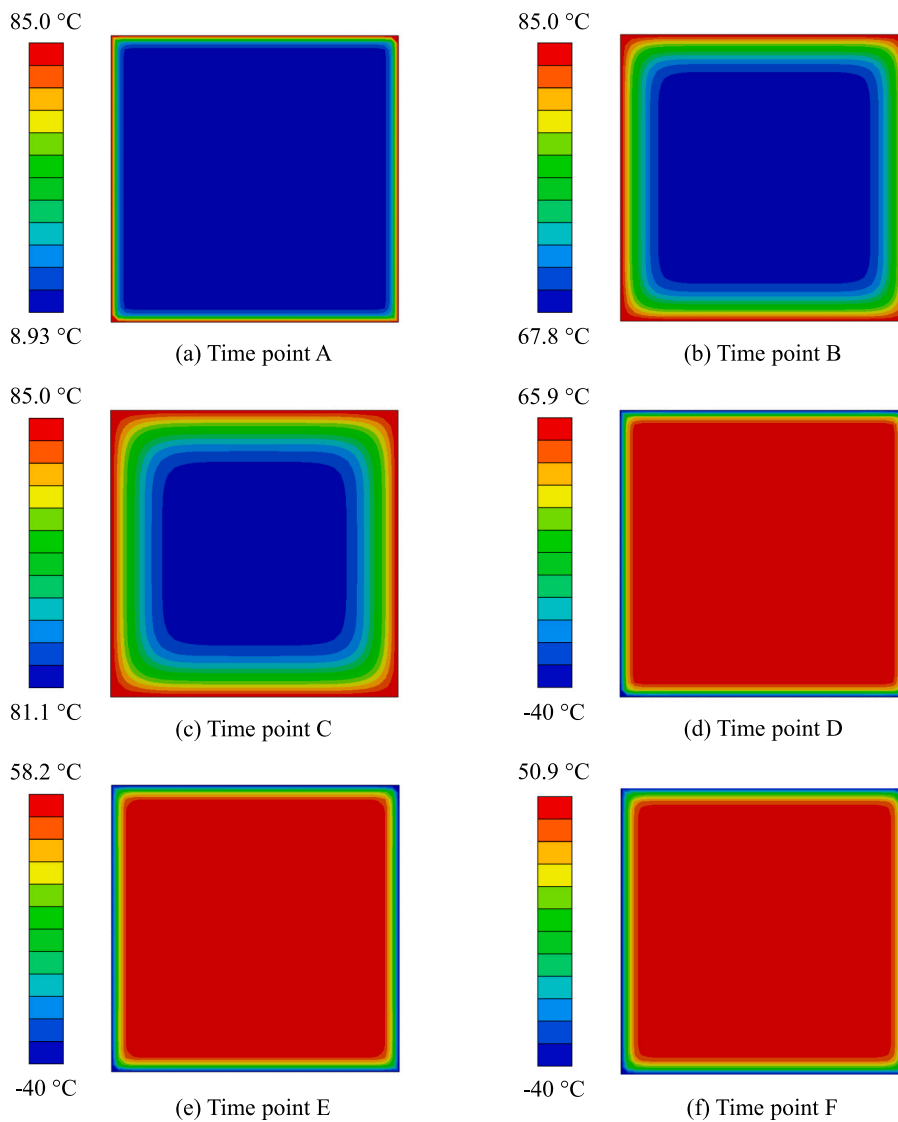


**Fig. 15.** The temperature contour plot inside EVA at six different time points in the first cycle during humidity freeze simulation.
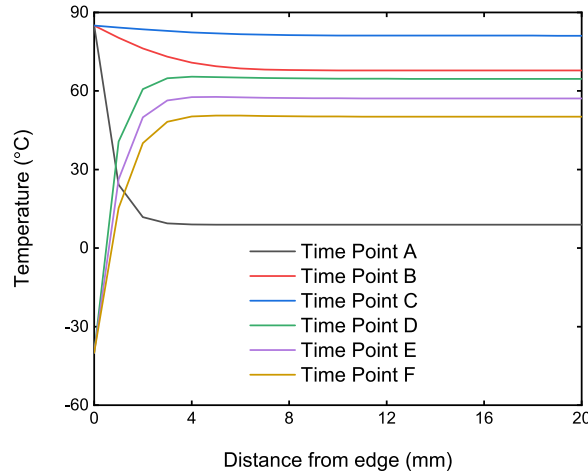
**Fig. 16.** The temperature versus distance from edge curves at six different time points in the first cycle during humidity freeze simulation.

where $\mathbf{N}_c = [N_1, N_2, N_3, N_4, N_5, N_6, N_7, N_8]$ is the shape function matrix, and $\tilde{\mathbf{c}}$ is the moisture concentration nodal vector. Besides, the interpolation of the spatial concentration gradient $\nabla_{\mathbf{X}} c$ and its variation $\nabla_{\mathbf{X}} \delta c$ can be expressed as

$$\nabla_{\mathbf{X}} c \approx \mathbf{G}^{-\mathrm{T}} \nabla_{\xi} \mathbf{N}_c \tilde{\mathbf{c}} = \mathbf{B}_c \tilde{\mathbf{c}}, \quad \nabla_{\mathbf{X}} \delta c \approx \mathbf{G}^{-\mathrm{T}} \nabla_{\xi} \mathbf{N}_c \delta \tilde{\mathbf{c}} = \mathbf{B}_c \delta \tilde{\mathbf{c}}, \tag{77}$$

Introducing Eqs. (76) and (77) into Eq. (75), the variational form of moisture diffusion is given by

$$\delta \tilde{\mathbf{c}}^{\mathrm{T}} \int_{B_0} \left( D \mathbf{B}_c^{\mathrm{T}} \nabla_{\mathbf{X}} c + \mathbf{N}_c^{\mathrm{T}} \dot{c} \right) \mathrm{d}\Omega = \delta \tilde{\mathbf{c}}^{\mathrm{T}} \mathbf{f}_{\mathrm{int}}^c \tag{78}$$

where $\mathbf{f}_{\mathrm{int}}^c$ is the internal residual vector, which is defined as

$$\mathbf{f}_{\mathrm{int}}^c = \int_{B_0} \left( D \mathbf{B}_c^{\mathrm{T}} \nabla_{\mathbf{X}} c + \mathbf{N}_c^{\mathrm{T}} \dot{c} \right) \mathrm{d}\Omega. \tag{79}$$

The linearization for moisture diffusion at the $(k+1)th$ iteration in the Newton–Raphson iterative solution scheme reads

$$\mathbf{K}^{c,k} \Delta \tilde{\mathbf{c}}^{k+1} = -\mathbf{f}_{\mathrm{int}}^{c,k} \tag{80a}$$

$$\tilde{\mathbf{c}}^{k+1} = \tilde{\mathbf{c}}^k + \Delta \tilde{\mathbf{c}}^{k+1} \tag{80b}$$

where $\mathbf{K}^c$ is the element stiffness for moisture diffusion, which is given by

$$\mathbf{K}^c = \int_{B_0} \left( D \mathbf{B}_c^{\mathrm{T}} \mathbf{B}_c + \frac{1}{\Delta t} \mathbf{N}_c^{\mathrm{T}} \mathbf{N}_c \right) \mathrm{d}\Omega \tag{81}$$

## 4. Staggered solution scheme for the multi-field framework

In this section, the staggered computational procedure for the solution of the thermo-mechanical problem with solid shell elements and interface finite elements, along with temperature-dependent 3D moisture diffusion, is outlined.

With regard to the thermo-mechanical governing equations incorporating the solid shell formulation, let consider the time increment $\left[ t_n, t_{n+1}^{(k)} \right]$, where $t_n$ and $t_{n+1}^{(k)}$ stand for the previous converged increment and prospective current increment at iteration k, respectively. Given the data $\{\mathbf{d}_n, \varsigma_n, \hat{\mathbf{T}}_n\}$ at the previous converged increment, the nonlinear incremental solution requires the Newton iterations at the intermediate state $\{\mathbf{d}_{n+1}^{(k)}, \varsigma_{n+1}^{(k)}, \hat{\mathbf{T}}_{n+1}^{(k)}\}$. Note that $\{\mathbf{d}_n, \varsigma_n, \hat{\mathbf{T}}_n\}$ and $\{\mathbf{d}_{n+1}^{(k)}, \varsigma_{n+1}^{(k)}, \hat{\mathbf{T}}_{n+1}^{(k)}\}$ denote the nodal displacement vector, the enhancing vector, and the nodal temperature vector at the previous converged increment and prospective current increment at $(k)th$ iteration, respectively. Based on the static condensation described in Section 3.1, the nodal displacement and temperature vectors are defined as unknowns in the element level, and the increment of enhancing vector in the $(k)th$ iteration of next time increment, $\Delta \varsigma_{n+1}^{(k)}$, should be determined. According to the procedure proposed in Reinoso and Blázquez (2016), $\Delta \zeta_{n+1}^{(k)}$ is given by

$$\Delta \varsigma_{n+1}^{(k)} = -\left[ \mathbf{k}_{\varsigma\varsigma,n} \right]^{-1} \left[ \mathbf{R}_{\mathrm{int},n}^{\varsigma} + \mathbf{k}_{\varsigma d,n} \Delta \mathbf{d}_{n+1}^{(k)} + \mathbf{k}_{\varsigma T,n} \Delta \hat{\mathbf{T}}_{n+1}^{(k)} \right] \tag{82}$$

It should be pointed out that the increments $\Delta \mathbf{d}_{n+1}^{(k)}$ and $\Delta \hat{\mathbf{T}}_{n+1}^{(k)}$ are provided by the solver, while the element matrices at the previous increment $\left[ \mathbf{k}_{\varsigma\varsigma,n} \right]^{-1}$, $\mathbf{R}_{\mathrm{int},n}^{\varsigma}$, $\mathbf{k}_{\varsigma d,n}$, $\mathbf{k}_{\varsigma T,n}$, and $\varsigma_n$ are all stored as internal variables. The numerical algorithm for the finite element
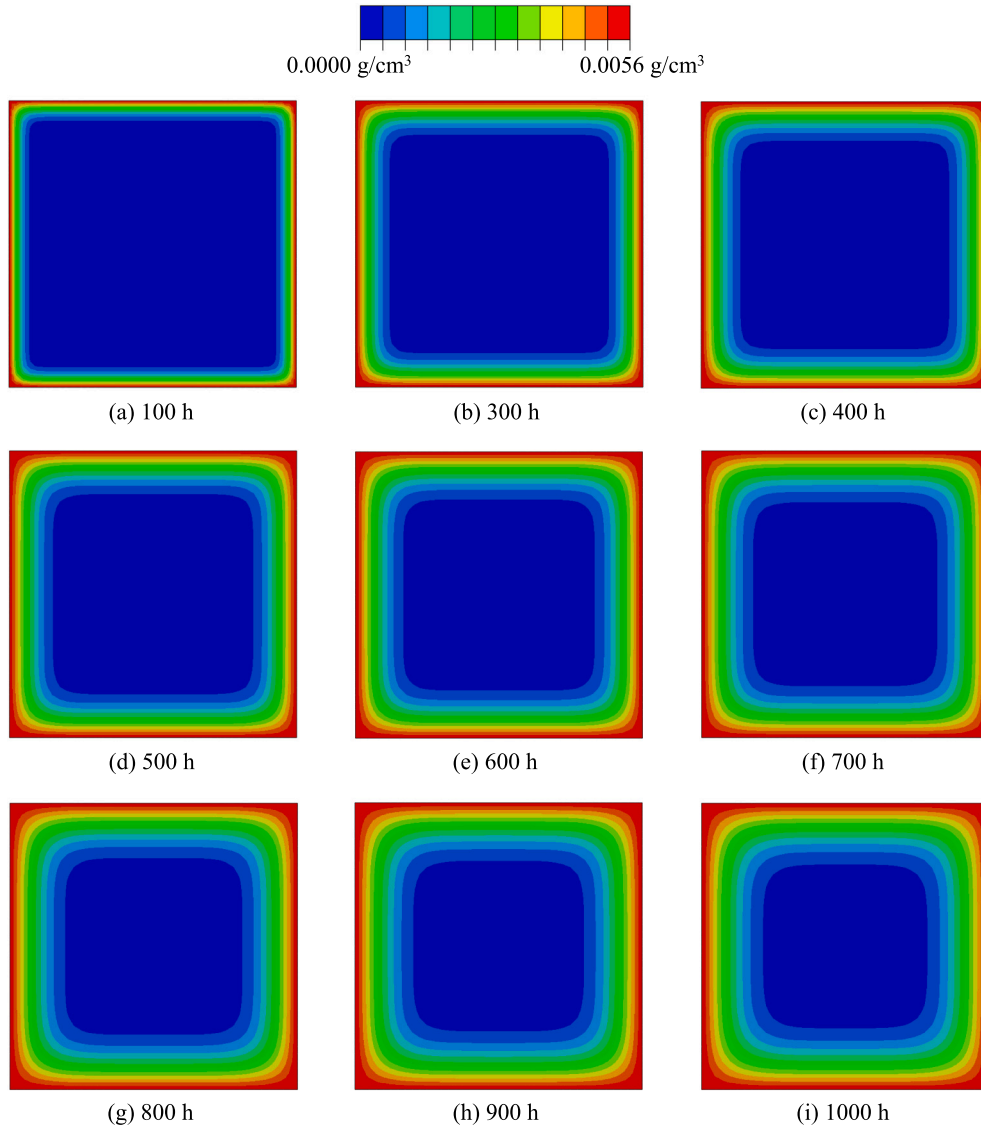
**Fig. 17.** The contour plot of moisture diffusion along the EVA layer during the humidity freeze simulation.

implementation of the thermo-mechanical problem with solid shell and interface element formulation is detailed in Algorithm 1. The Newton–Raphson iteration is performed until the machine precision is achieved, i.e., the tolerance of residual vector is up to $10^{-15}$.

It is worth noting that the history variables $h$ at the integration points need to be determined due to the time dependency of visco-elastic constitutive equation, Eq. (20). To model relaxation, this history variable is set to zero in case of any temperature change, which is stored as a state variable in the interface element implementation, while updated by the current time increment if the temperature value remains constant compared with that of previous increment, see Algorithm 1. Hence, the drawback of temperature–time superposition principle for thermo-visco-elastic modeling of polymeric materials is overcome.

Once the temperature and displacement field in the coupled thermo-mechanical problem are solved in a given time increment, these nodal values are transferred to the moisture diffusion problem, which is solved by the Euler backward time integration scheme using the same temporal interval with that of the thermo-mechanical analysis. As stated in Section 2.3, given the time scale difference between the moisture diffusion and thermo-mechanical phenomena, the coefficient in the current increment of moisture diffusion

analysis is determined from the nodal temperature and gap values at the previous time increment. The detailed computational procedure of moisture diffusion is outlined in Algorithm 2.

---

**Algorithm 1:** Numerical implementation procedure of the coupled thermo-mechanical formulation

---

**if** *Solid shell element* **then**

    **Data:** $\mathbf{d}_n$, $\hat{\mathbf{T}}_n$, $\Delta\mathbf{d}_{n+1}^{(k)}$, $\Delta\hat{\mathbf{T}}_{n+1}^{(k)}$

    **Result:** $\mathbf{d}_{n+1}$, $\hat{\mathbf{T}}_{n+1}$

    *Initialization of* $\varsigma_n$, $\mathbf{R}_{\mathrm{int},n}^{\varsigma}$, $\mathbf{k}_{\varsigma d,n}$, $\left[\mathbf{k}_{\varsigma\varsigma,n}\right]^{-1}$;

    **while** $||R_d^*|| > tolerance$ **do**

        *Compute* $\Delta\varsigma_{n+1}^{(k)} = -\left[\mathbf{k}_{\varsigma\varsigma,n}\right]^{-1}\left[\mathbf{R}_{\mathrm{int},n}^{\varsigma} + \mathbf{k}_{\varsigma d,n}\Delta\mathbf{d}_{n+1}^{(k)} + \mathbf{k}_{\varsigma T,n}\Delta\hat{\mathbf{T}}_{n+1}^{(k)}\right]$;

        *Update the enhancing vector* $\varsigma_{n+1}^{(k)} = \varsigma_n + \Delta\varsigma_{n+1}^{(k)}$;

        **for** $n \leftarrow 1$ **to** *8 integration points* **do**

            *Compute the curvilinear basis* $\mathbf{G}_{n+1}^{(k)}$ *and* $\mathbf{g}_{n+1}^{(k)}$;

            *Compute the B matrices* $\mathbf{B}_{n+1}^{(k)}$ *and* $\mathbf{B}_{T,n+1}^{(k)}$;

            *Modify the* $\mathbf{B}_{n+1}^{(k)}$ *matrix according to the ANS method*;

            *Compute* $\mathbb{C}_{n+1}^{(k)}$, $\mathbf{S}_{n+1}^{(k)}$, *and* $\mathbf{Z}_{n+1}^{(k)}$;

            *Compute the EAS operator* $\mathbf{M}_{n+1}^{(k)}$;

        **end**

        *Compute the element stiffness matrices* $\mathbf{k}_{dd,n+1}^{(k)}$, $\mathbf{k}_{d\varsigma,n+1}^{(k)}$, $\mathbf{k}_{\varsigma d,n+1}^{(k)}$, $\mathbf{k}_{\varsigma\varsigma,n+1}^{(k)}$, *and* $\mathbf{k}_{TT,n+1}^{(k)}$;

        *Compute the internal force vectors* $\mathbf{R}_{\mathrm{int},n+1}^{d(k)}$, $\mathbf{R}_{\mathrm{int},n+1}^{\varsigma(k)}$, *and* $\mathbf{R}_{\mathrm{int},n+1}^{T(k)}$;

        *Perform the static condensation and final assembly*;

    **end**

**end**

**else if** *Cohesive interface element* **then**

    **Data:** $\mathbf{d}_n$, $\hat{\mathbf{T}}_n$, $\Delta\mathbf{d}_{n+1}^{(k)}$, $\Delta\hat{\mathbf{T}}_{n+1}^{(k)}$

    **Result:** $\mathbf{d}_{n+1}$, $\hat{\mathbf{T}}_{n+1}$

    **while** $||R_d^*|| > tolerance$ **do**

        *Compute the operators* $\mathbf{L}_{cz}$ *and* $\mathbf{M}_{cz}$;

        **for** $n \leftarrow 1$ **to** *4 integration points* **do**

            *Compute the shape function* $\mathbf{N}_{cz,n+1}^{(k)}$;

            *Compute the matrix* $\mathbf{B}_{cz,n+1}^{(k)} = \mathbf{N}_{cz,n+1}^{(k)}\mathbf{L}_{cz}$;

            *Compute the rotation matrix in the curvilinear system* $\mathbf{R}_{cz,n+1}^{(k)}$;

            *Compute the local gap* $\mathbf{g}_{\mathrm{loc},n+1}^{(k)} = \mathbf{R}_{cz,n+1}^{(k)}\mathbf{B}_{cz,n+1}^{(k)}\hat{\mathbf{d}}_{n+1}^{(k)}$;

            *Compute the temperature value at the integration point* $T_{int,n+1}^{(k)}$;

            **if** $|T_{int,n+1}^{(k)} - T_{int,n}| > tolerance$ **then**

                *Compute the history variable* $h_{int,n+1}^{(k)} = h_{int,n}$;

            **else**

                *Compute the history variable* $h_{int,n+1}^{(k)} = h_{int,n} + \Delta t$;

            **end**

            *Compute the stiffness matrix* $\mathbf{C}_{cz,n+1}^{(k)}$ *and the traction vector* $\mathbf{T}_{n+1}^{(k)}$;

        **end**

        *Compute the element stiffness matrix* $\mathbf{K}_{\mathrm{int},n+1}^{e(k)}$;

        *Compute the internal residual vector* $\mathbf{f}_{\mathrm{int},n+1}^{(k)}$;

    **end**

**end**

---

---

**Algorithm 2:** Numerical implementation procedure of the moisture diffusion along the interface

---

**Data:** $\tilde{\mathbf{c}}_n$, $\Delta \tilde{\mathbf{c}}_{n+1}^{(k)}$
**Result:** $\tilde{\mathbf{c}}_{n+1}$
*Initialization of* $\mathbf{d}_n$ *and* $\hat{\mathbf{T}}_n$;
**while** $\|\mathbf{f}_{int}^c\| > tolerance$ **do**
    **for** $n \leftarrow 1$ to 8 *integration points* **do**
        *Compute the shape function* $\mathbf{N}_{c,n+1}^{(k)}$;
        *Compute the B matrix* $\mathbf{B}_{c,n+1}^{(k)}$;
        *Compute the temperature value at the integration point* $T_{int,n}$ *with* $\hat{\mathbf{T}}_n$;
        *Compute the normal gap at the integration point* $\Delta_{int,n}$ *with* $\mathbf{d}_n$;
        **if** $\Delta_{int,n} \leq \delta_n^c$ **then**
            *Compute the coefficient* $D_{int,n+1}^{(k)} = A \exp\left(-\frac{E_a}{T_{int,n} R}\right)$;
        **else**
            *Compute the coefficient* $D_{int,n+1}^{(k)} = A \exp\left(-\frac{E_a}{T_{int,n} R}\right) \frac{\Delta_{int,n}}{\delta_n^c}$;
        **end**
    **end**
    *Compute the element stiffness matrices* $\mathbf{K}_{c,n+1}^{(k)}$;
    *Compute the internal force vectors* $\mathbf{f}_{int,n+1}^{c(k)}$;
    *Perform the final assembly*;
**end**

---

## 5. Numerical applications to photovoltaics

In this section, three international standard tests for photovoltaics, including damp heat test, humidity freeze test, and thermal cycling test, are simulated by the proposed computational framework. Note that the damp heat test requires constant temperature and humidity testing environments, which uncouples the moisture diffusion from the thermo-mechanical problem and thus allows the derivation of analytical solution useful for benchmark targets, while the latter require the fully coupled solution scheme due to the spatial variation of temperature. Besides, the role of cracks in silicon on moisture diffusion pattern is also investigated and compared with experimental electroluminescence images.

### 5.1. Damp heat test

As prescribed by the international standard, the damp heat test is conducted in the environmental chamber with the constant temperature of 85 °C and relative humidity of 85% RH. This humidity environmental condition corresponds to the initial boundary condition with a moisture concentration $c^* = 0.0056$ g/cm$^3$ imposed on the free edges of the photovoltaic laminate. Since temperature is kept constant in this test, the moisture diffusion problem can be solved independently from the coupled thermo-mechanical problem with a constant diffusivity.

In this work, the specimen is a double-glass PV laminate of span $l = 40$ mm separated by EVA. The thickness of glass laminae is 3 mm, and the thickness of EVA is 0.5 mm. As glass is not permeable, the moisture will only diffuse from the free edges of EVA towards the central part in this test, see Fig. 9. The analytical solution was obtained in Crank (1979), which will be treated as a benchmark of the computational scheme proposed above. Assuming the initial laminate is dry, the spatial and temporal solution $c$ can be obtained as

$$c = c^* + \frac{4c^*}{\pi} \sum_{m=0}^{\infty} \frac{1}{2m+1} \sin\left[\frac{(2m+1)\pi x}{l}\right] e^{\left(-D(2m+1)^2 \pi^2 t / l^2\right)} \tag{83}$$

The mesh size of finite element model is 1 mm, and there are 1600 solid diffusion elements in total. The contour plot of moisture concentration inside the EVA is shown in Fig. 10 and, as clearly seen, water concentration gradually diffuses from the edges into the middle area of EVA during simulation. At 100 h, the most area of EVA is still dry with almost zero concentration, see Fig. 10(a), while after 1000 h, the dry area becomes obviously smaller. To quantitatively validate the computational diffusion model, the predicted moisture concentration with respect to the distance from the edge after 1000 h (the black solid line in Fig. 11) is compared with that obtained from the analytical solution (the black dotted line in Fig. 11), and they agree with each other very well. Besides, this model is also used to simulate the experimental results obtained from Miami as reported in Kempe (2006), and numerical predictions also agree very well with the data from the impermeable double-glass laminate exposed to Miami environment for 1 year, 2 years, and 3 years, which further proves the reliability of the diffusion modeling method proposed in this work.
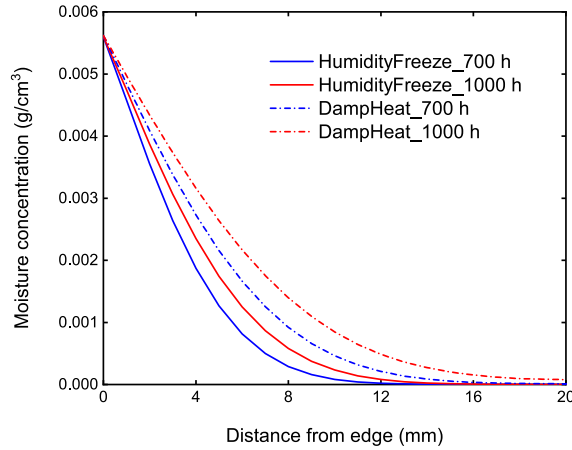
**Fig. 18.** The comparison of moisture concentration versus distance from edge curves after 700 h and 1000 h between the damp heat and humidity freeze simulations.
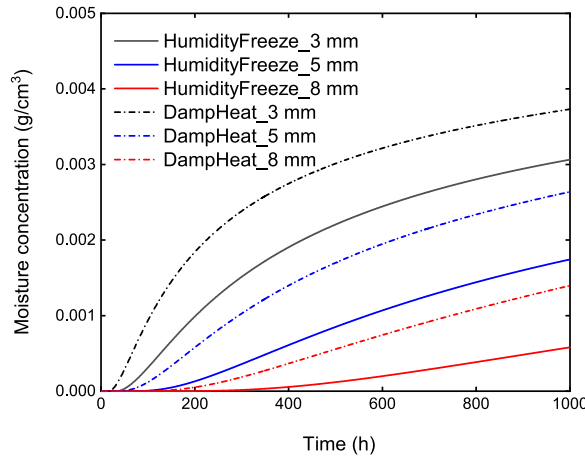


**Fig. 19.** The comparison of time history of moisture concentration at the positions 3 mm, 5 mm, and 8 mm away from the edge between the damp heat and humidity freeze simulations.

### 5.2. Humidity freeze test

In the humidity freeze test of PV laminates, as requested by the international standard, the modules are subjected to the cycling temperature condition from −40 °C to 85 °C with the constant humidity condition of 85% RH. The temperature ramp can be expressed as

$$
T^*(t) = \begin{cases}
\frac{t}{t_1^*}T_1^* & 0 \le t < t_1^* \\
T_1^* & t_1^* \le t < t_2^* \\
\frac{t_3^*-t}{t_3^*-t_2^*}T_1^* & t_2^* \le t < t_3^* \\
\frac{t-t_3^*}{t_4^*-t_3^*}T_2^* & t_3^* \le t < t_4^* \\
T_2^* & t_4^* \le t < t_5^* \\
\frac{t_6^*-t}{t_6^*-t_5^*}T_2^* & t_5^* \le t < t_6^*
\end{cases}
\tag{84}
$$

where $T_1^* = 85$ °C, $T_2^* = -40$ °C, and $t_1^* = 1.0$ h, $t_2^* = 21.0$ h, $t_3^* = 22.0$ h, $t_4^* = 22.5$ h, $t_5^* = 23.5$ h, $t_6^* = 24.0$ h, as shown in Fig. 12.

Compared with the damp heat test, this case is much more complex and almost impossible to obtain the analytical solution due to the spatial and temporal temperature variation inside the EVA, to which a non-constant temperature boundary condition is applied. Particularly, the cohesive properties and diffusivity of EVA need to be updated during simulation, and to be specific, the viscoelastic parameters $\alpha(T)$ and $a(T)$ for the calibration of Young's modulus of EVA are temperature dependent as experimentally
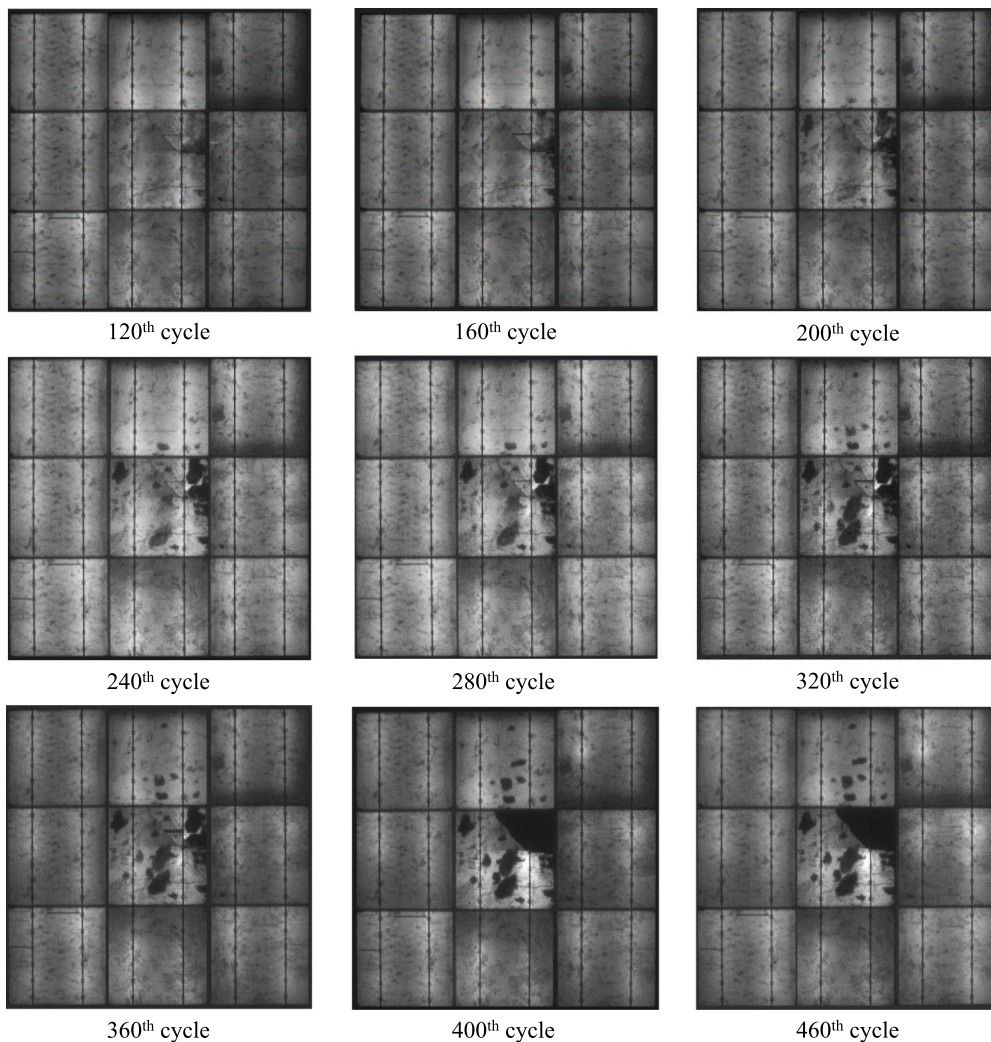
**Fig. 20.** EL images of the minimodule taken at different cycles during the thermal cycling test.
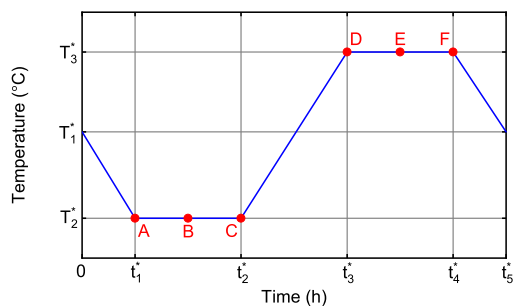*Source:* Adapted from Berardone and Paggi (2019).



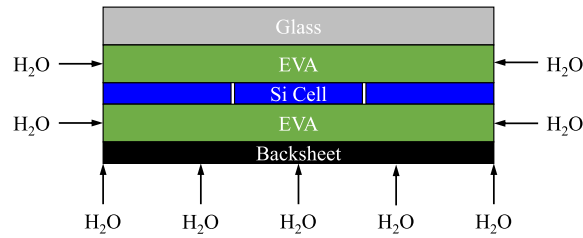**Fig. 21.** Temperature profile imposed inside the chamber during the thermal cycling test.

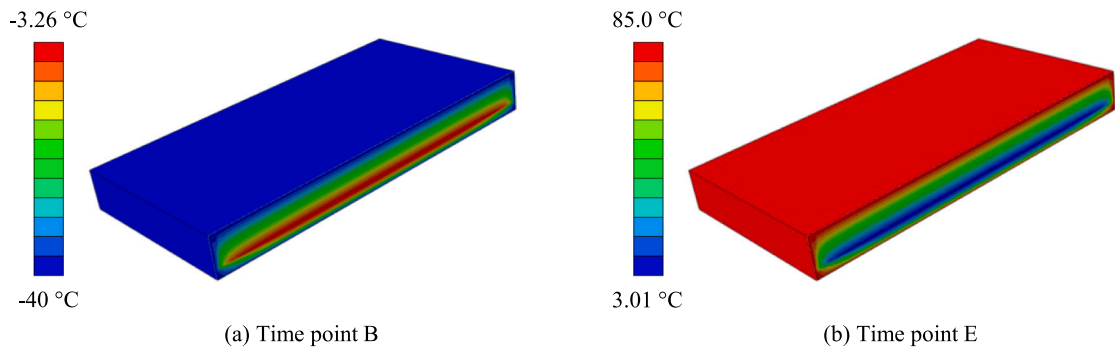**Fig. 22.** The sketch of the PV minimodule in the thermal cycling test.



(a) Time point B

(b) Time point E

**Fig. 23.** The temperature contour plot of the cross section of the minimodule at time points B and E in the first cycle during the thermal cycling test.

**Table 1**
Mechanical and thermal properties of the PV materials.

|  | $E$ (GPa) | $\rho$ (kg/m³) | $\alpha$ | $c_p$ (J/kg K) | $k_0$ (W/m K) |
| --- | --- | --- | --- | --- | --- |
| Backsheet | 2.8 | 1000 | 5.04e-5 | 300 | 0.36 |
| Glass | 73 | 2300 | 8e-6 | 500 | 0.8 |
| Silicon | 130 | 2500 | 2.49e-6 | 715 | 148 |

evaluated in Paggi et al. (2011) and interpreted through the fractional calculus method (Sapora and Paggi, 2014), see the plot of modulus $E$, $a(T)$, and $\alpha(T)$ in Fig. 13. Regarding the properties of moisture diffusion, the coefficient $D$ is determined according to the Arrhenius type equation Eq. (24) reported in Kempe (2006). The thermal and mechanical properties of different PV materials are taken from Eitner et al. (2011), Paggi et al. (2011), which are listed in Table 1. Besides, the critical opening of polymeric interface $\delta_n^c$ can be estimated from the experimental data of variation of Mode 1 fracture energy with respect to temperature in Novoa et al. (2014), since the area below the traction versus separation curve is the fracture energy.

The temperature variation inside the double glass laminate is strongly dependent on the heat conduction properties of different layers, as shown by the temperature contour of the cross-section at time point A in Fig. 14. The contour plot of temperature distribution inside the EVA layer in the first cycle during simulation is shown in Fig. 15. At time point A, the boundary temperature reaches 85 °C, and is kept constant for 20 h. As shown in Fig. 15(a)–(c), heat gradually diffuses from the edges into the middle area of EVA during this period. At time point D, the boundary temperature drops to −40 °C, but the temperature in the middle area of EVA layer is still higher than 65 °C due to the inertial effect of heat conduction, see Fig. 15(d)–(f). Remarkably, this spatial and temporal variation of temperature inside EVA leads to the difference of moisture diffusion properties from that of EVA subjected to constant condition in the damp heat test. To quantitatively describe the spatial variation of temperature inside EVA, the temperature versus distance from edge curves at the six different time points in the first cycle is plotted in Fig. 16. As can be seen, the plateau value, which corresponds to the central area temperature of EVA, gradually goes up from time point A to C with the evolution of thermal conduction. At time C, the temperature at almost all the area of EVA from the edge to the center reaches around 85 °C, which means the EVA layer is fully and evenly heated after 20 h. Besides, the plateau at the time period when boundary temperature changes to −40 °C, which can be ascribed to the hysteresis of heat conduction, gradually goes down from time point D to F. It is worth noting that the temperature at the central area is still higher than 30 °C at the end of one complete cycle due to the relatively short duration of constant low-temperature boundary loading.

The contour plot history of moisture diffusion during the humidity freeze simulation is shown in Fig. 17. The moisture gradually diffuses into the central area, which is very similar to the phenomena obtained from previous damp heat simulation. However, the
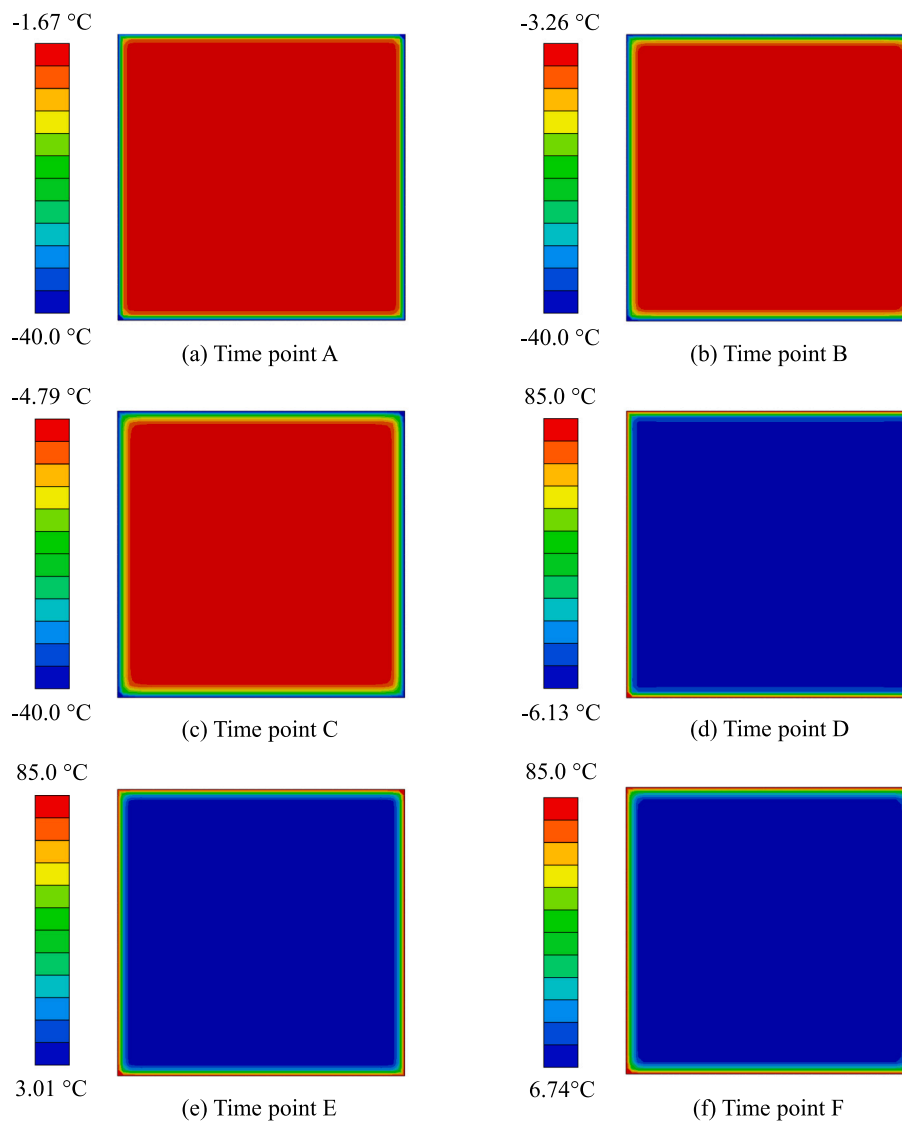
**Fig. 24.** The temperature contour plot inside EVA at six different time points in the first cycle during thermal cycling simulation.

amount of moisture concentration is totally different in two cases due to the spatial variation of temperature inside EVA in the humidity freeze simulation. As shown in Fig. 18, the difference of moisture concentration spatial variation after 700 h and 1000 h between the damp heat and humidity freeze simulation can be observed. Note that the amount of moisture concentration in all the area of EVA after 700 h and 1000 h in the damp heat case is higher than that in the humidity freeze case, since the moisture diffusion coefficient in the former case is much higher at the constant high-temperature condition (85 °C). Furthermore, It can be seen from Fig. 18 that the amount of moisture concentration at all the areas of EVA after 700 h in the damp heat case is even higher than that in the humidity freeze case after 1000 h, which further demonstrates the effect of temperature on moisture diffusion. Besides the difference of spatial variation, the temporal variation between the damp heat and humidity freeze simulation is also shown and compared in this work, see Fig. 19. The time history of moisture concentration at three positions 3 mm, 5 mm, and 8 mm away from the edge is also plotted, and the curves obtained from the damp heat simulations (solid lines) are higher than all the counterparts obtained from the humidity freeze simulations (dotted lines). Thus, conclusions can be drawn that temperature plays an import role on the moisture diffusion problem as the coefficient is determined from the Arrhenius equation, and this coupling can be described with the proposed modeling method, which can be demonstrated by the example of humidity freeze simulation.
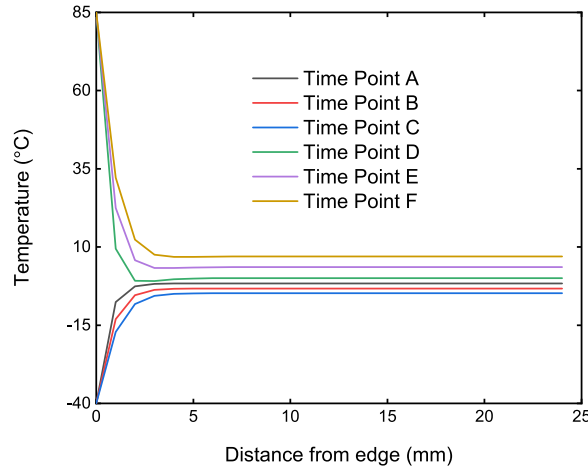
**Fig. 25.** The temperature versus distance from edge curves at six different time points in the first cycle during thermal cycling simulation.

### 5.3. Thermal cycling test

In this section, as shown in Fig. 20, a minimodule composed of $3 \times 3$ multicrystalline solar cells with a crack in the middle one, which was tested under the thermal cycling environmental condition with EL images taken regularly as reported in Berardone and Paggi (2019), was simulated using the proposed modeling framework. In this case, the temperature ramp is given by

$$T^*(t) = \begin{cases} \frac{t_1^* - t}{t_1^*}(T_1^* - T_2^*) + T_2^* & 0 \leq t < t_1^* \\ T_2^* & t_1^* \leq t < t_2^* \\ \frac{t - t_2^*}{t_3^* - t_2^*}(T_3^* - T_2^*) + T_2^* & t_2^* \leq t < t_3^* \\ T_3^* & t_3^* \leq t < t_4^* \\ \frac{t_5^* - t}{t_5^* - t_4^*}(T_3^* - T_1^*) + T_1^* & t_4^* \leq t < t_5^* \end{cases} \tag{85}$$

where $T_1^* = 25\ °C$, $T_2^* = -40\ °C$, $T_3^* = 85\ °C$, and $t_1^* = 0.5$ h, $t_2^* = 1.5$ h, $t_3^* = 2.5$ h, $t_4^* = 3.5$ h, $t_5^* = 4.0$ h, as shown in Fig. 21. The sketch of the cross-section of the PV minimodule is shown in Fig. 22. The module consists of a tempered glass with the thickness of 4 mm, an encapsulating EVA with the thickness of 0.5 mm, the silicon solar cell with the thickness of 0.166 mm, another layer of EVA, and finally a thin backsheet made of an ethylene tetrafluoroethylene core and silicon nitride coating with the thickness of 0.1 mm. The thermal and mechanical properties of all the component materials are listed in Table 1. The size of this PV module is 48 cm, and the adopted mesh size of the finite element model is 1 mm. Since backsheet is permeable to water and thus moisture can penetrate from it and percolates along the edges of each solar cell, it is admissible in the numerical simulation to directly impose moisture boundary condition at the edges of each solar cell embedded in the module, see Fig. 22.

The temperature contour plots of the cross-section of the minimodule at time point B and time point E are shown in Fig. 23. Owning to the different heat conductivity properties of different layers (glass, backsheet, and silicon solar cells), the temperature inside the PV minimodule presents significant spatial variation at both the cooling and heating stages. The temperature distribution inside the EVA layer of the module at six time points of the first cycle during the thermal cycling simulation is shown in Fig. 24. At time point A, heat has diffused inside the panel. From time point A to C, the thermal boundary condition is kept constant with the temperature of 85 °C, and as can be clearly seen, the EVA layer is almost fully heated at the end of this heating period. When the temperature boundary condition drops to −40 °C at time point D, this layer starts cooling down from its edges, but the temperature in the most area is still very high after this period, and the lowest temperature is up to around 50 °C in the time point F, see Fig. 24(f). This trend is quantified in Fig. 25 by plotting the temperature versus the distance from edge at six time points during the first cycle. Compared with the previous curves obtained from humidity freeze simulation, the platforms are relatively lower at the temperature level of around 0 °C because of the much shorter heating period with the constant temperature boundary condition 85 °C.

The contour plots of moisture concentration inside the EVA layer above the silicon solar cell layer during the thermal cycling simulation are shown in Fig. 26. Notably, moisture diffusion can take place not only from the edges of the module, but also along the interspaces between different solar cells as well as the crack indicated in Fig. 20. Thus the moisture boundary condition $c^*$ is imposed on all these edges, and the numerical simulation is performed with this computational framework. As pointed out in Wolters (1980), the moisture plays a significant role in the oxidation of silicon solar cell, which is demonstrated by the observed darkness in the EL images shown in Fig. 20. The silicon oxidation versus time history curves at the different moisture concentration are plotted in Fig. 27, and it can be seen that higher moisture concentration and longer exposure time lead to more silicon oxidation.
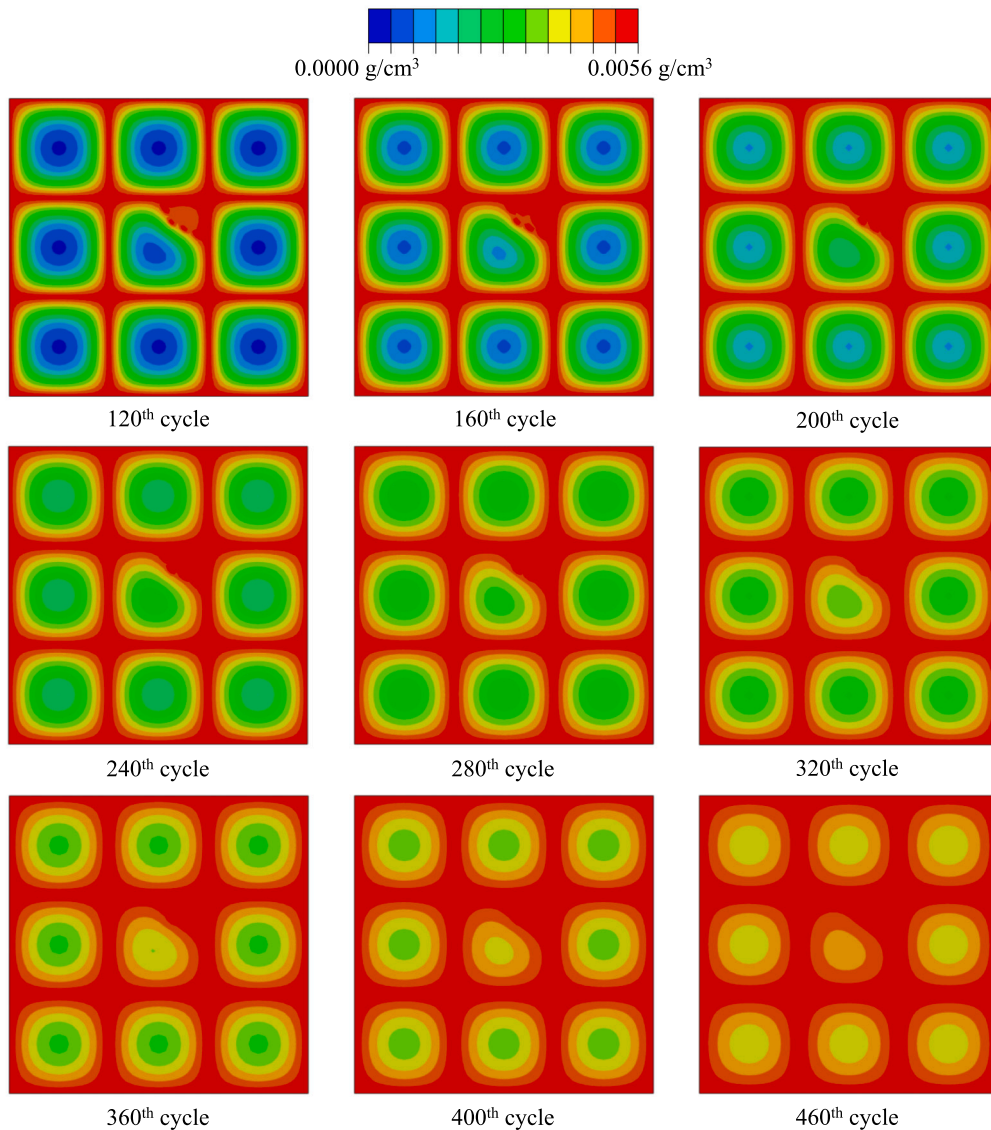
**Fig. 26.** The contour plot of moisture diffusion along the EVA layer above the silicon solar cell layer during the thermal cycling simulation.

The contour plots of normalized oxidation of the minimodule during the thermal cycling simulation are shown in Fig. 28. The area close to the crack of the middle solar cell starts becoming deeply oxidized resulting from moisture intrusion while all other cell areas show much lower degradation, which demonstrates the consistency between simulation and experiment. At the 460th cycle, as shown in Fig. 28, the upper right area of the middle solar cell during simulation is almost fully oxidized due to the moisture intrusion from the crack channel, and the corresponding EL image (see Fig. 20) also shows much dimmer area at the same position compared with that at the previous cycle. At this stage, electric degradation is significantly enhanced by moisture diffusion from the crack channels and the corresponding oxidation. The contour plots of oxidation (see Fig. 28) correlates very well with the EL images in terms of the electrically inactive area, which is a comparison impossible to be achieved by analytical methods.

## 6. Conclusions

In this work, a comprehensive 3D finite element computational framework has been established for the modeling of hygro-thermo-visco-elastic problems in the thin-walled photovoltaic laminate with polymeric interface. To simulate the thermo-mechanical response of the very thin laminae in the PV module, the consistent derivation of solid shell element formulation incorporating the EAS and ANS methods to alleviate the different locking pathologies is proposed. Besides, a 3D thermo-mechanical interface element formulation is developed to model the polymeric encapsulant layers between different laminae with a traction–separation
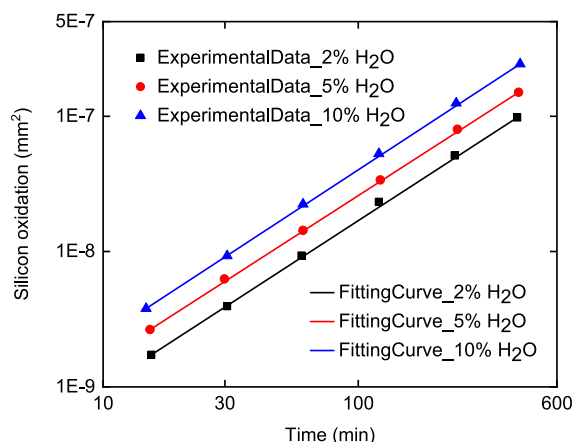
**Fig. 27.** The silicon oxidation versus time history for different moisture concentrations.
*Source:* Adapted from Wolters (1980).

constitutive law using the fractional calculus method for the description of rheologically complex thermo-visco-elastic behavior. Moreover, given the difference of time scales between the moisture diffusion and thermo-mechanical problems, a staggered scheme is proposed to solve the partial differential equations governing the thermo-elastic and heat transfer problems in different laminae and polymeric interfaces, and then update the diffusion coefficient in the moisture diffusion analysis as well as its subsequent solution.

The computational methodology is successfully applied to the simulation of three standard qualification tests requested by the International Electrotechnical Commission, namely the damp heat test, humidity freeze test, and thermal cycling test. In the damp heat case, the numerical prediction is compared with the analytical solution together with experimental data from Miami, and good consistency proves the validity of the modeling method. To see the difference of moisture diffusion with and without thermo-mechanical coupling, the simulation of temperature dependent moisture diffusion in the humidity freeze case with cyclic temperature boundary condition is performed and compared with the previous damp heat simulation, which shows the capabilities of the proposed methodology for the modeling of spatial and temporal variation of moisture concentration inside the EVA layer. Finally, the thermal cycling test of a PV minimodule with a central crack in the middle solar cell is also simulated with a different cyclic temperature boundary condition from that of the humidity freeze test, and the predicted trend of crack enhanced moisture diffusion is experimentally validated with the electric degradation EL images taken at different stages. With this proposed computational tool at hand, it is possible to numerically perform the durability analysis of PV modules under different complex environmental conditions and thus open new possibilities for the design of more reliable products in the PV industry. The problem of EVA swelling could be considered in the future work to extend the present computational framework to simulate photovoltaics recycling. A potential research path could regard the development of the computational framework in Hajikhani et al. (2021) developed for hydrogels, which needs to be extended to EVA and the solvents used for PV recycling.

## Declaration of competing interest

The authors declare that they have no known competing financial interests or personal relationships that could have appeared to influence the work reported in this paper.

## Data availability

Data will be made available on request.
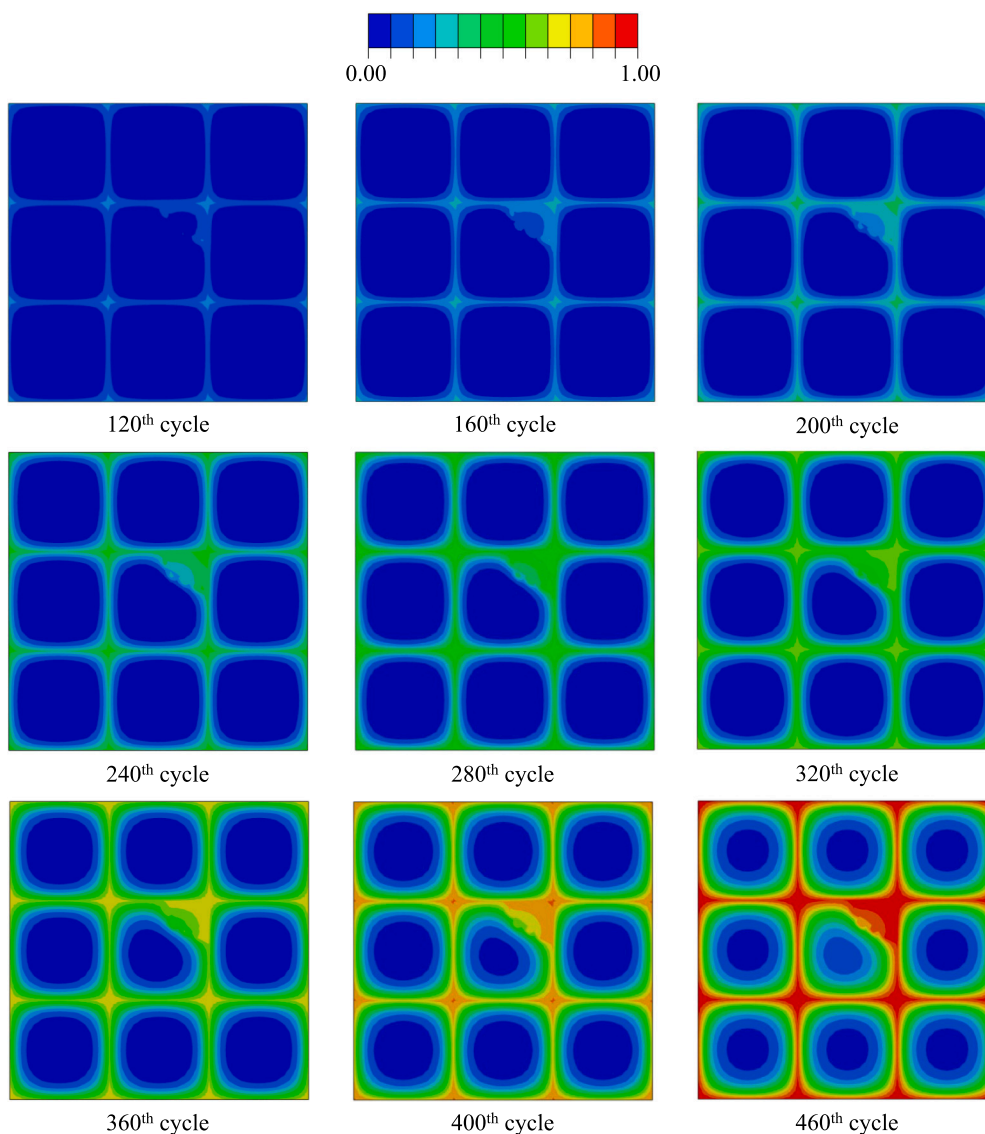
## Acknowledgments

**Fig. 28.** The contour plot of normalized silicon oxidation of the minimodule during the thermal cycling simulation.

# References

Antartis, D., Chasiotis, I., 2014. Residual stress and mechanical property measurements in amorphous Si photovoltaic thin films. Sol. Energy 105, 694–704.

Bahrololoumi, A., Morovati, V., Poshtan, E.A., Dargazany, R., 2020. A multi-physics constitutive model to predict hydrolytic aging in quasi-static behaviour of thin cross-linked polymers. Int. J. Plast. 130, 102676.

Bahrololoumi, A., Morovati, V., Shaafaey, M., Dargazany, R., 2021. A multi-physics approach on modeling of hygrothermal aging and its effects on constitutive behavior of cross-linked polymers. J. Mech. Phys. Solids 156, 104614.

Bargmann, S., Steinmann, P., 2006. Theoretical and computational aspects of non-classical thermoelasticity. Comput. Methods Appl. Mech. Engrg. 196 (1–3), 516–527.

Başar, Y., Ding, Y., 1997. Shear deformation models for large-strain shell analysis. Int. J. Solids Struct. 34 (14), 1687–1708.

Bathe, K.-J., Dvorkin, E.N., 1985. A four-node plate bending element based on Mindlin/Reissner plate theory and a mixed interpolation. Internat. J. Numer. Methods Engrg. 21 (2), 367–383.

Berardone, I., Paggi, M., 2019. Nondestructive monitoring of damage caused by accelerated ageing in photovoltaic modules. Proc. Inst. Mech. Eng., Part C: J. Mech. Eng. Sci. 233 (23–24), 7565–7572.

Betsch, P., Gruttmann, F., Stein, E., 1996. A 4-node finite shell element for the implementation of general hyperelastic 3D-elasticity at finite strains. Comput. Methods Appl. Mech. Engrg. 130 (1–2), 57–79.

Betsch, P., Stein, E., 1995. An assumed strain approach avoiding artificial thickness straining for a non-linear 4-node shell element. Commun. Numer. Methods. Eng. 11 (11), 899–909.

Bischoff, M., Ramm, E., 1997. Shear deformable shell elements for large strains and rotations. Internat. J. Numer. Methods Engrg. 40 (23), 4427–4449.

Brank, B., 2005. Nonlinear shell models with seven kinematic parameters. Comput. Methods Appl. Mech. Engrg. 194 (21–24), 2336–2362.

Braun, M., Bischoff, M., Ramm, E., 1994. Nonlinear shell formulations for complete three-dimensional constitutive laws including composites and laminates. Comput. Mech. 15 (1), 1–18.

Büchter, N., Ramm, E., Roehl, D., 1994. Three-dimensional extension of non-linear shell formulation based on the enhanced assumed strain concept. Internat. J. Numer. Methods Engrg. 37 (15), 2551–2568.

Cardoso, R.P., Yoon, J.W., Mahardika, M., Choudhry, S., Alves de Sousa, R., Fontes Valente, R., 2008. Enhanced assumed strain (EAS) and assumed natural strain (ANS) methods for one-point quadrature solid-shell elements. Internat. J. Numer. Methods Engrg. 75 (2), 156–187.

Corrado, M., Paggi, M., 2015. Nonlinear fracture dynamics of laminates with finite thickness adhesives. Mech. Mater. 80, 183–192.

Crank, J., 1979. The Mathematics of Diffusion. Oxford University Press.

Deng, G., Ma, W., Peng, Y., Wang, S., Yao, S., Peng, S., 2021. Experimental study on laminated glass responses of high-speed trains subject to windblown sand particles loading. Constr. Build. Mater. 300, 124332.

Di Paola, M., Pinnola, F.P., Zingales, M., 2013. A discrete mechanical model of fractional hereditary materials. Meccanica 48 (7), 1573–1586.

Di Paola, M., Pirrotta, A., Valenza, A., 2011. Visco-elastic behavior through fractional calculus: An easier method for best fitting experimental results. Mech. Mater. 43 (12), 799–806.

Dunlop, E.D., 2003. Lifetime performance of crystalline silicon PV modules. In: 3rd World Conference on Photovoltaic Energy Conversion, 2003. Proceedings, Vol. 3. IEEE, pp. 2927–2930.

Dvorkin, E.N., Bathe, K.-J., 1984. A continuum mechanics based four-node shell element for general non-linear analysis. Eng. Comput..

Eitner, U., Kajari-Schröder, S., Köntges, M., Altenbach, H., 2011. Thermal stress and strain of solar cells in photovoltaic modules. In: Shell-Like Structures. Springer, pp. 453–468.

Gagliardi, M., Paggi, M., 2019. Multiphysics analysis of backsheet blistering in photovoltaic modules. Sol. Energy 183, 512–520.

Gruttmann, F., Wagner, W., 2006. Structural analysis of composite laminates using a mixed hybrid shell element. Comput. Mech. 37 (6), 479–497.

Hajikhani, A., Wriggers, P., Marino, M., 2021. Chemo-mechanical modelling of swelling and crosslinking reaction kinetics in alginate hydrogels: A novel theory and its numerical implementation. J. Mech. Phys. Solids 153, 104476.

Harnau, M., Schweizerhof, K., 2002. About linear and quadratic "solid-shell" elements at large deformations. Comput. Struct. 80 (9–10), 805–817.

Hauptmann, R., Schweizerhof, K., Doll, S., 2000. Extension of the 'solid-shell' concept for application to large elastic and large elastoplastic deformations. Internat. J. Numer. Methods Engrg. 49 (9), 1121–1141.

Herrmann, W., Bogdanski, N., 2011. Outdoor weathering of PV modules—effects of various climates and comparison with accelerated laboratory testing. In: 2011 37th IEEE Photovoltaic Specialists Conference. IEEE, pp. 002305–002311.

Iseghem, M., Plotton, A., Penneau, J., Chatagnon, N., Binesti, D., 2012. Failure modes after damp heat tests on PV modules. In: Proceedings of the 27th European Photovoltaic Solar Energy Conference and Exhibition. pp. 3546–3548.

Kasper, E.P., Taylor, R.L., 2000. A mixed-enhanced strain method: Part II: Geometrically nonlinear problems. Comput. Struct. 75 (3), 251–260.

Kempe, M.D., 2006. Modeling of rates of moisture ingress into photovoltaic modules. Sol. Energy Mater. Sol. Cells 90 (16), 2720–2738.

Klinkel, S., Gruttmann, F., Wagner, W., 2006. A robust non-linear solid shell element based on a mixed variational formulation. Comput. Methods Appl. Mech. Engrg. 195 (1–3), 179–201.

Klinkel, S., Wagner, W., 1997. A geometrical non-linear brick element based on the EAS-method. Internat. J. Numer. Methods Engrg. 40 (24), 4529–4545.

Köntges, M., Kurtz, S., Packard, C., Jahn, U., Berger, K.A., Kato, K., Friesen, T., Liu, H., Van Iseghem, M., Wohlgemuth, J., et al., 2014. Review of Failures of Photovoltaic Modules. International Energy Agency, IEA-PVPS, Task 13, ISBN: 978-3-906042-16-9.

Köntges, M., Oreski, G., Jahn, U., Herz, M., Hacke, P., Weiss, K.-A., Razongles, G., Paggi, M., Parlevliet, D., Tanahashi, T., et al., 2017. Assessment of Photovoltaic Module Failures in the Field. International Energy Agency, IEA-PVPS, Task 13, ISBN: 978-3-906042-54-1.

Korelc, J., Wriggers, P., 1996. Consistent gradient formulation for a stable enhanced strain method for large deformations. Eng. Comput. 13, 103–123.

Kuhl, E., Denzer, R., Barth, F.J., Steinmann, P., 2004. Application of the material force method to thermo-hyperelasticity. Comput. Methods Appl. Mech. Engrg. 193 (30–32), 3303–3325.

Lenarda, P., Paggi, M., 2016. A geometrical multi-scale numerical method for coupled hygro-thermo-mechanical problems in photovoltaic laminates. Comput. Mech. 57 (6), 947–963.

Lenarda, P., Paggi, M., 2022. A computational framework for rheologically complex thermo-visco-elastic materials. Int. J. Solids Struct. 236, 111297.

Liu, Z., Reinoso, J., Paggi, M., 2022a. A humidity dose-CZM formulation to simulate new end-of-life recycling methods for photovoltaic laminates. Eng. Fract. Mech. 259, 108125.

Liu, Z., Reinoso, J., Paggi, M., 2022b. Phase field modeling of brittle fracture in large-deformation solid shells with the efficient quasi-newton solution global–local approach. Comput. Methods Appl. Mech. Engrg. 399, 115410.

Liu, Z., Xia, Y., 2019. Development of a numerical material model for axial crushing mechanical characterization of woven CFRP composites. Compos. Struct. 230, 111531.

Liu, Z., Xia, Y., 2021. Numerical and experimental investigation on mechanical responses of plain woven CFRP composite under various loading cases. Int. J. Crashworthiness 26 (1), 65–76.

Liu, Z., Xia, Y., Guo, S., 2019. Characterization methods of delamination in a plain woven CFRP composite. J. Mater. Sci. 54 (20), 13157–13174.

Mainardi, F., 2010. An introduction to mathematical models. In: Fractional Calculus and Waves in Linear Viscoelasticity. Imperial College Press, London.

Miehe, C., 1998. A theoretical and computational model for isotropic elastoplastic stress analysis in shells at large strains. Comput. Methods Appl. Mech. Engrg. 155 (3–4), 193–233.

Novoa, F.D., Miller, D.C., Dauskardt, R.H., 2014. Environmental mechanisms of debonding in photovoltaic backsheets. Sol. Energy Mater. Sol. Cells 120, 87–93.

Novoa, F.D., Miller, D.C., Dauskardt, R.H., 2016. Adhesion and debonding kinetics of photovoltaic encapsulation in moist environments. Prog. Photovolt., Res. Appl. 24 (2), 183–194.

Paggi, M., Corrado, M., Berardone, I., 2016. A global/local approach for the prediction of the electric response of cracked solar cells in photovoltaic modules under the action of mechanical loads. Eng. Fract. Mech. 168, 40–57.

Paggi, M., Corrado, M., Rodriguez, M.A., 2013. A multi-physics and multi-scale numerical approach to microcracking and power-loss in photovoltaic modules. Compos. Struct. 95, 630–638.

Paggi, M., Kajari-Schröder, S., Eitner, U., 2011. Thermomechanical deformations in photovoltaic laminates. J. Strain Anal. Eng. Des. 46 (8), 772–782.

Paggi, M., Sapora, A., 2015. An accurate thermoviscoelastic rheological model for ethylene vinyl acetate based on fractional calculus. Int. J. Photoenergy 2015.

Parisch, H., 1995. A continuum-based shell theory for non-linear applications. Internat. J. Numer. Methods Engrg. 38 (11), 1855–1883.

Rah, K., Paepegem, W.V., Habraken, A.-M., Degrieck, J., De Sousa, R., Valente, R., 2013. Optimal low-order fully integrated solid-shell elements. Comput. Mech. 51 (3), 309–326.

Reinoso, J., Blázquez, A., 2016. Application and finite element implementation of 7-parameter shell element for geometrically nonlinear analysis of layered CFRP composites. Compos. Struct. 139, 263–276.

Reinoso, J., Blázquez, A., Estefani, A., París, F., Cañas, J., Arévalo, E., Cruz, F., 2012. Experimental and three-dimensional global-local finite element analysis of a composite component including degradation process at the interfaces. Composites B 43 (4), 1929–1942.

Reinoso, J., Paggi, M., 2014. A consistent interface element formulation for geometrical and material nonlinearities. Comput. Mech. 54 (6), 1569–1581.

Sapora, A., Paggi, M., 2014. A coupled cohesive zone model for transient analysis of thermoelastic interface debonding. Comput. Mech. 53 (4), 845–857.

Schwarze, M., Reese, S., 2009. A reduced integration solid-shell finite element based on the EAS and the ANS concept—geometrically linear problems. Internat. J. Numer. Methods Engrg. 80 (10), 1322–1355.

Silberstein, M.N., Boyce, M.C., 2010. Constitutive modeling of the rate, temperature, and hydration dependent deformation response of Nafion to monotonic and cyclic loading. J. Power Sources 195 (17), 5692–5706.

Silberstein, M.N., Boyce, M.C., 2011. Hygro-thermal mechanical behavior of Nafion during constrained swelling. J. Power Sources 196 (7), 3452–3460.

Simo, J.-C., Armero, F., 1992. Geometrically non-linear enhanced strain mixed methods and the method of incompatible modes. Internat. J. Numer. Methods Engrg. 33 (7), 1413–1449.

Simo, J., Armero, F., Taylor, R., 1993. Improved versions of assumed enhanced strain tri-linear elements for 3D finite deformation problems. Comput. Methods Appl. Mech. Engrg. 110 (3–4), 359–386.

Simo, J.C., Rifai, M., 1990. A class of mixed assumed strain methods and the method of incompatible modes. Internat. J. Numer. Methods Engrg. 29 (8), 1595–1638.

Simo, J., Rifai, M., Fox, D., 1990. On a stress resultant geometrically exact shell model. Part IV: Variable thickness shells with through-the-thickness stretching. Comput. Methods Appl. Mech. Engrg. 81 (1), 91–126.

Valente, R., Jorge, R., Cardoso, R.P., César de Sá, J., Grácio, J.J., 2003. On the use of an enhanced transverse shear strain shell element for problems involving large rotations. Comput. Mech. 30 (4), 286–296.

Vu-Quoc, L., Tan, X., 2003. Optimal solid shells for non-linear analyses of multilayer composites. I. Statics. Comput. Methods Appl. Mech. Engrg. 192 (9–10), 975–1016.

Weber, G., Anand, L., 1990. Finite deformation constitutive equations and a time integration procedure for isotropic, hyperelastic-viscoplastic solids. Comput. Methods Appl. Mech. Engrg. 79 (2), 173–202.

Wolters, D., 1980. On the oxidation kinetics of silicon: The role of water. J. Electrochem. Soc. 127 (9), 2072.